Monthly Notices of the ROYAL ASTRONOMICAL SOCIETY

MNRAS **533,** 572–588 (2024)
Advance Access publication 2024 July 24

https://doi.org/10.1093/mnras/stae1786

Dark energy survey year 3 results: miscentring calibration and X-ray-richness scaling relations in redMaPPer clusters

P. M. Kelly [1,2★] J. Jobel [1] O. Eiger [1,3,4] A. Abd [1,5] T. E. Jeltema [1,3★] P. Giles [6] D. L. Hollowood [1,3] R. D. Wilkinson [6] D. J. Turner [6] S. Bhargava [6,7] S. Everett [8] A. Farahi [9] A. K. Romer [6] E. S. Rykoff [10,11] F. Wang [12,13] S. Bocquet [14] D. Cross [15] R. Faridjoo,[16] J. Franco,[1] G. Gardner,[1] M. Kwiecien [1,3] D. Laubner [1,17] A. McDaniel,[18] J. H. O'Donnell [1,3] L. Sanchez,[19] E. Schmidt,[1] S. Sripada,[20] A. Swart,[21] E. Upsdell [6] A. Webber,[18] M. Aguena,[22] S. Allam,[23] O. Alves,[24] D. Bacon,[25] D. Brooks,[26] D. L. Burke,[10,11] A. Carnero Rosell,[22,27,28] J. Carretero,[29] C. A. Collins,[30] M. Costanzi,[31,32,33] L. N. da Costa,[22] M. E. S. Pereira,[34] T. M. Davis,[35] P. Doel,[26] I. Ferrero,[36] J. Frieman,[23,37] J. García-Bellido,[38] G. Giannini,[29] D. Gruen,[14] R. A. Gruendl,[39,40] M. Hilton,[41] S. R. Hinton,[35] K. Honscheid,[42,43] D. J. James,[44] K. Kuehn,[45,46] R. G. Mann,[47] J. L. Marshall,[48] J. Mena-Fernández,[49] C. J. Miller,[50] R. Miquel,[29,51] J. Myles,[10,11,52] A. Palmese,[53] A. Pieres,[22,54] A. A. Plazas Malagón,[10,11] P. J. Rooney,[6] M. Sahlen,[55] E. Sanchez,[49] D. Sanchez Cid,[49] M. Schubnell,[24] I. Sevilla-Noarbe,[49] M. Smith,[56] J. P. Stott,[57] E. Suchyta,[57] M. E. C. Swanson,[39] G. Tarle,[24] C. To,[42] P. T. P. Viana,[58,59] N. Weaverdyck,[24,60] and P. Wiseman[56] (DES Collaboration)

Affiliations are listed at the end of the paper

Accepted 2024 July 11. Received 2024 June 20; in original form 2023 September 29

ABSTRACT

We use Dark Energy Survey Year 3 (DES Y3) clusters with archival *XMM–Newton* and *Chandra* X-ray data to assess the centring performance of the redMaPPer cluster finder and to measure key richness observable scaling relations. We find that 10–20 per cent of redMaPPer clusters are miscentred, both when comparing to the X-ray peak position and to the visually identified central cluster galaxy. We find no significant difference in miscentring in bins of low versus high richness or redshift. The dominant reasons for miscentring include masked or missing data and the presence of other bright galaxies in the cluster. For half of the miscentred clusters, the correct central was one of the possible centrals identified by redMaPPer, while for ∼40 per cent of miscentred clusters, the correct central is not a redMaPPer member mostly due to masking. Additionally, we fit scaling relations of X-ray temperature and luminosity with richness. We find a T_X–λ scatter of 0.21 ± 0.01. While the scatter in T_X–λ is consistent in redshift bins, we find modestly different slopes, with high-redshift clusters displaying a somewhat shallower relation. Splitting based on richness, we find a marginally larger scatter for our lowest richness bin, $20 < \lambda < 40$. We note that the robustness of the scaling relations at lower richnesses is limited by the unknown selection function, but at $\lambda > 75$, we detect nearly all of the clusters falling within existing X-ray pointings. The X-ray properties of detected, serendipitous clusters are generally consistent with those of targeted clusters.

Key words: galaxies: clusters: general – galaxies: clusters: intracluster medium – X-rays: galaxies: clusters.

1 INTRODUCTION

The formation and evolution of galaxy clusters depend sensitively on the expansion history and matter density of the Universe, and the growth of the cluster mass function with cosmic time can be used to constrain the dark energy equation of state (e.g. Allen, Evrard & Mantz 2011; Weinberg et al. 2013; Huterer & Shafer 2018). With the advent of wide-field surveys such as the Dark Energy Survey (DES) and the Legacy Survey of Space and Time (LSST), optical cluster surveys can provide strong constraints on cosmology (e.g. Weinberg et al. 2013; Abbott et al. 2020). The very large cluster samples in these surveys enable excellent statistical constraints, making control and calibration of systematics in cluster selection and characterization of the utmost importance.

The cluster finder employed by the DES for cosmological analyses, redMaPPer (Rykoff et al. 2014), is a red sequence based algorithm for identifying clusters. RedMaPPer has been shown to have excellent redshift performance, and its richness estimator, λ, has low intrinsic scatter with cluster mass (Rozo et al. 2009). The DES Y1 (year 1)

★ E-mail: pmkelly@ucdavis.edu (PMK); tesla@ucsc.edu (TEJ)

cluster cosmology sample included a total of 7066 clusters in the volume-limited, $\lambda > 20$ catalogue. The DES Y3 (years 1–3) $\lambda > 20$, volume-limited cluster catalogue forming the basis of this work in comparison contains 21 092 clusters. Abbott et al. (2020) showed that the combination of cluster number counts and stacked cluster weak lensing in DES has the statistical potential to equal or exceed the constraining power of the DES 3×2 pt combined analysis. However, even for DES Y1, the cluster analysis is systematics limited, and more specifically, these results imply the presence of unmodelled systematics for low-richness clusters.

Aspects of redMaPPer selection, like miscentring and projection effects, as well as richness scatter, can be probed using multi-wavelength follow up and spectroscopy. Previous work has derived estimates for both the richness-mass scatter and miscentring fractions using Sunyaev–Zeldovich effect (SZ; Saro et al. 2015; Bleem et al. 2020), X-ray (Rykoff et al. 2016; Hollowood et al. 2019; Kirby et al. 2019; Zhang et al. 2019; Farahi et al. 2019b; Giles et al. 2022), and weak-lensing (WL; Mantz et al. 2016; Mulroy et al. 2019) observations of redMaPPer clusters in SDSS, DES Science Verification (SV), and DES Y1. Where available, spectroscopy has been used to probe projection effects and the velocity dispersion – richness relation (Farahi et al. 2016; Myles et al. 2021; Wetzell et al. 2022). Myles et al. (2021) measure the fraction of observed richness contributed by non-cluster galaxies seen in projection for SDSS redMaPPer clusters; they find projection fractions generally consistent with the current DES models (Costanzi et al. 2019) but with a strong trend of increasing projection for decreasing richness. In addition, SZ observations favour a different slope to the mass-richness relation than found with stacked WL and hint at scatter or contamination that grows at low richness (Bleem et al. 2020; Costanzi et al. 2021; Grandis et al. 2021).

While the work of Farahi et al. (2019b), Zhang et al. (2019), and Hollowood et al. (2019) provides valuable X-ray follow-up and calibration for the DES cluster sample, previous studies are limited by small sample sizes and particularly by small samples of low-richness clusters and 'serendipitous' clusters (clusters that are not imaged as the aimpoint of an X-ray follow-up observation). Likewise, current SZ samples are limited to high-richness clusters ($\lambda > 40$). In this paper, we present X-ray scaling relations and mis-centring distributions for the DES Y3 clusters which have archival *Chandra* or *XMM–Newton* observations, including richness and redshift trends. We also explore the reasons for miscentring and the miscentring induced richness bias. After flag and redshift cuts, our sample includes 676 unique clusters with X-ray observations of which 243 have high signal-to-noise detections; 82 of these detected clusters have richnesses $\lambda < 40$.

In Section 2, we briefly summarize the DES data and cluster catalogue. Section 3 presents both the *Chandra* and *XMM* data reduction, analysis, and X-ray cluster selection criteria. In Section 4, we present our results for both cluster centring and X-ray-richness scaling relations in addition to discussing aspects of cluster selection and centring informed by the X-ray data. Throughout the paper, we assume a flat ΛCDM cosmological model with matter density $\Omega_{\rm M} = 0.3$, Hubble constant $H_0 = 70\,{\rm km\,s^{-1}\,Mpc^{-1}}$, and $E(z)$, the dimensionless Hubble parameter as a function of redshift, defined as $E(z) = \frac{H(z)}{H_0} = \sqrt{\Omega_M(1+z)^3 + 1 - \Omega_{\rm M}}$.

2 DES DATA AND CLUSTER SELECTION

2.1 DES Y3 data

In this work, we characterize the X-ray properties of clusters selected from the DES three year data set (DES Y3). DES Y3 includes data acquired between 2013 August 15 and 2016 February 12 using the Dark Energy Camera (DECam Flaugher et al. 2015) mounted on the Blanco 4m telescope at the Cerro Tololo Interamerican observatory in Chile. Though the DES Y3 GOLD data covers significantly more area than the DES Y1 GOLD data, it is generally not deeper. The DES Y3 GOLD catalogue includes 388 million objects imaged in 4946 square degrees of the sky in the g, r, i, and z broad-band filters (Sevilla-Noarbe et al. 2021). This is a significant increase compared to the 1786 square degrees of sky included in the Y1 GOLD catalogue from the first year of data (Drlica-Wagner et al. 2018).

2.2 RedMaPPer

The red-sequence Matched-filter Probabilistic Percolation, or redMaPPer, cluster finding algorithm (Rykoff et al. 2014) has proven to be a powerful tool for selecting clusters from optical photometric survey data based on the cluster red sequence and has been applied to SDSS, DES Science Verification, and DES Y1 data (Rykoff et al. 2014, 2016; McClintock et al. 2019). The redMaPPer algorithm iteratively self-trains the red sequence model using available spectroscopic redshifts and, furthermore, iteratively calculates photometric redshifts for each cluster found. Starting from a potential central cluster galaxy, potential cluster galaxies are given a membership probability using a matched-filter algorithm with filters for spatial position, colour, and magnitude. This process is iterative with final membership probabilities determined relative to the most likely central galaxy. Up to five potential central galaxies are identified and given probabilities of being the cluster centre. The richness (λ) of each redMaPPer cluster is calculated as the sum of membership probabilities over all galaxies within a scale radius R_λ, where $R_\lambda = 1.0h^{-1}{\rm Mpc}(\lambda/100)^{0.2}$.

The cluster catalogue used in this work was generated by redMaPPer v6.4.22+2 run on the DES Y3 data (Y3A2 Gold 2.2.1). The analysis in this paper was restricted to clusters in the volume-limited, $\lambda > 20$ catalogue containing 21 092 clusters. We further limit the catalogue to clusters in the redshift range $0.2 < z < 0.65$ adopted for DES cluster cosmology studies.

3 X-RAY ANALYSIS

Starting from the DES Y3 redMaPPer cluster catalogue, we utilize available, archival *Chandra* and *XMM–Newton* data at redMaPPer cluster positions to determine cluster X-ray properties including temperature, luminosity, X-ray centres, and luminosity upper limits for undetected clusters. The X-ray data reduction and analysis are presented below for *Chandra* and *XMM* data in Sections 3.1 and 3.2, respectively. The analysis methods used and additional tests of these have been presented in previous papers (Hollowood et al. 2019; Zhang et al. 2019; Farahi et al. 2019b; Giles et al. 2022), and here we summarize the relevant procedures.

Table 1 provides a summary of the *Chandra* and *XMM* samples used in this work, as outlined in Sections 3.1 and 3.2. Sample sizes for subsamples studied are noted in the corresponding tables in Sections 4 and 5.

3.1 *Chandra* sample and analysis

We analyse archival *Chandra* data for redMaPPer clusters using the **MATCha** (**M**ass **A**nalysis **T**ool for **Cha**ndra) pipeline as introduced in Hollowood et al. (2019). Given a cluster catalogue containing a set of equatorial coordinates (RA, Dec) and a redshift (z), MATCha automatically downloads any *Chandra* data which includes

Table 1. Summary of the X-ray samples used in this work and their median redshift, richness, and X-ray temperatures.

Sample	$N_{\rm sam}$	$z_{\rm med}$	$\lambda_{\rm med}$	$T_{\rm X,med}$ [keV]
Chandra (centring)	124	0.39	98	7.11
Chandra ($T_{\rm X,r_{2500}}$)	98	0.40	105	7.23
XMM ($T_{\rm X,r_{2500}}$)	161	0.39	47	3.96

these coordinates. It then attempts to find X-ray temperatures and luminosities (T_X, L_X) as well as cluster centroids and X-ray peaks. MATCha performs this analysis by running a series of CIAO (version 4.10 and CALDB version 4.8.1) (Fruscione et al. 2006) and HEASOFT (version 6.24) tools[1] (Blackburn et al. 1999). In this section, we outline the data preparation and analysis in the MATCha algorithm and post-processing steps.

3.1.1 *MATCha analysis*

MATCha first queries the *Chandra* data base for data overlapping the *redMaPPer* cluster positions using the CIAO tool *find_chandra_obsid*. MATCha then downloads each set of *Chandra* observations and reduces them using the CIAO tool *chandra_repro*. We narrow the energy range to 0.3–7.9 keV and remove particle background flares using the CIAO tool *deflare* before creating images and exposure maps for each observation. MATCha identifies point sources using the CIAO tool *wavdetect* and removes them from the data.

MATCha then attempts to measure $T_{\rm X}$, $L_{\rm X}$, centroids, and X-ray peaks. MATCha iteratively attempts to find a centroid within a 500 kpc region with the initial centre at the redMaPPer position and with subsequent iterations centred at the most recent centroid. If no stable centre is found within 20 iterations, MATCha marks the cluster as 'undetected' and outputs an upper limit on $L_{\rm X}$ using the redMaPPer position. Clusters whose signal-to-noise ratios are less than 5 within the final 500 kpc region are also marked as 'undetected'. Otherwise, the cluster is marked as 'detected', and we extract a spectrum within the 500 kpc radius using the CIAO tool *specextract*.

For detected clusters, we first fit $L_{\rm X}$ and $T_{\rm X}$ within the 500 kpc aperture using XSPEC (Arnaud 1996) assuming a column density of galactic neutral hydrogen from the HEASOFT tool, $n_{\rm H}$ (this is a weighted average of the hydrogen densities found in Kalberla et al. (2005) and Dickey & Lockman (1990)). Cluster spectra are fit using XSPEC's wabs∗mekal model. The abundance is fixed to $0.3 Z_{\odot}$, a value typical for X-ray clusters (Kravtsov & Borgani 2012), using the solar abundances from Anders & Grevesse (1989). If the fit is successful, this process is repeated for additional aperture sizes, and centroids $T_{\rm X}$ and $L_{\rm X}$ are found for r_{2500}, r_{500}, and core-cropped r_{500} apertures (core size of $0.15 r_{500}$). These regions are also found iteratively, with initial guesses for r_{2500} calculated from the 500 kpc $T_{\rm X}$ and initial guesses for r_{500} calculated from the $r_{2500} T_{\rm X}$. Here, r_{δ} refers to the radius at which the mean mass density is δ times the critical density at the cluster redshift, and r_{δ} is estimated using the temperature-radius relations in Arnaud, Pointecouteau & Pratt (2005).

For clusters that are detected but for which the temperature fit failed, MATCha will still estimate the luminosity. In this case, the luminosity within a 500 kpc aperture is determined at a fixed temperature with iteration on the assumed $T_{\rm X}$ using an $L_{\rm X}$–$T_{\rm X}$ relation to guess the temperature based on the measured luminosity. Initially, the luminosity is determined for a starting $T_{\rm X}$ of 3 keV; the temperature guess is updated based on the $L_{\rm X}$–$T_{\rm X}$ relation, and the luminosity determined for the new temperature. This process is repeated until $L_{\rm X}$ is unchanged within the uncertainties. In this work, we use an $L_{\rm X}$–$T_{\rm X}$ relation based on previous fits to *Chandra* observations of SDSS redMaPPer clusters (Hollowood et al. 2019). 500 kpc is roughly equivalent to r_{2500} for our clusters (Hollowood et al. 2019). For undetected clusters, we estimate a 3σ upper limit on $L_{\rm X}$ within a 500 kpc aperture with an assumed $T_{\rm X} = 3$ keV.

MATCha additionally determines X-ray peaks for detected clusters by determining the brightest pixel in smoothed, exposure-corrected, point source subtracted images. Images are smoothed using a $\sigma =$ 50 kpc Gaussian.

3.1.2 *Post processing*

Several problematic cases or failure modes of the automated analysis are identified in the post processing. These include instances in which most of the cluster source or background regions are not in *Chandra*'s field of view and clusters for which *Chandra* was not in an imaging mode when all images were taken. Separate flags were used for proximity to chip edges affecting determination of the X-ray centre, r_{2500}, r_{500}, or background properties. Clusters where a second nearby cluster significantly contaminated the emission or background were additionally flagged. We also check that no detected clusters are actually bright nearby clusters rather than the intended *redMaPPer* cluster by comparing the output cluster catalogue to the NASA/IPAC Extragalactic Database[2] as well as other redMaPPer clusters in the field. These clusters are flagged as 'masked' and cut from the sample.

Post-processing visual analysis is also required to check the locations of the X-ray peak positions. If the centres are incorrect due to point-source emission, the point-source subtraction is adjusted and the centre corrected. Mispercolations (as detailed in Hollowood et al. 2019) are identified visually and corrected by assigning the higher richness in redMaPPer to the more luminous X-ray cluster. The less luminous cluster is flagged as masked and removed from the sample. In practice, there was only one such case in the Y3 Chandra sample. For a second rich cluster in the sample, the X-ray position was misidentified as a $\lambda < 20$ cluster; we simply treat this cluster as miscentred.

3.1.3 *Chandra samples and flag cuts*

There were 415 clusters from the volume-limited, $\lambda > 20$ Y3 redMaPPer catalogue within $0.2 < z < 0.65$ falling with archival *Chandra* data. Of these, 186 clusters were detected. We further restrict this sample based on signal-to-noise ratio (SNR), as this improves the centring accuracy and decreases the point source contamination. Specifically, we remove clusters with a SNR in a 500 kpc aperture less than 9.0, which was determined to be a good minimum for both the *Chandra* and *XMM* samples, cutting 46 clusters. In addition, for determination of the X-ray scaling relations, we removed clusters flagged as masked by another cluster, bad (non-imaging) mode, lying too close to a chip edge for robust determination of the X-ray temperature or background, and clusters where another nearby cluster significantly contaminated the emission sampled in either the cluster or background regions. In total, an additional 27 clusters

[1] https://heasarc.gsfc.nasa.gov/ftools/

[2] https://ned.ipac.caltech.edu/ The NASA/IPAC Extragalactic Database (NED) is funded by the National Aeronautics and Space Administration and operated by the California Institute of Technology.

were removed by the flag cuts, leaving 113 clusters. For 15 of these clusters, we were unable to fit an r_{2500} temperature due to poor statistics in the spectrum, leaving a final sample of 98 clusters used to fit the $T_{X,r2500}$–λ scaling relation. For the r_{500} aperture, the same flags were applied with the only difference in cuts being two clusters where an r_{500} temperature could not be fit, leaving 96 clusters to be used in the T_X–λ fit for an r_{500} region.

For cluster X-ray luminosity and the determination of the L_X–λ relations, there are several different cases to consider. We utilize the measured luminosities for 113 clusters with SNR > 9 and meeting the same flag cuts above, of which 98 have a measured T_X and 15 have luminosities determined using an estimated T_X from iteration on the L_X–T_X relation. For both undetected clusters and detected clusters with SNR < 9, we utilize only upper limits on the luminosity and include these data as censored in fits of the L_X–λ relation. This category includes 183 undetected clusters and 17 clusters with $5 <$ SNR < 9, giving a total of 313 clusters in the luminosity sample.

Less restrictive cuts were used for the centring analysis in Section 4, as here it was only necessary that the X-ray peak position could be robustly determined. The same cuts for SNR, masking, and bad mode were used, but clusters near chip edges were only flagged if the cluster was close enough to the edge to affect peak determination, and clusters with neighbouring clusters were only flagged if the nearby cluster was within the r_{2500} region. These cuts gave a total sample of 124 clusters for the centring analysis.

3.2 XCS sample and analysis

Here, we describe the construction of the DES Y3 cluster sample cross-matched with available *XMM* data. The *XMM* data are made available from the XMM cluster survey (XCS; Romer et al. 2001). The aim of XCS is to catalogue and analyse all X-ray clusters detected during the XMM mission. The XCS data used in this work comprises all publicly available *XMM* observations as of April 2019.[3] Much of the process outlined here is detailed in Giles et al. (2022), with the main matching and analysis process briefly described below.

3.2.1 *XMM reduction, image generation, and source detection*

The XCS reduction process is fully described in Lloyd-Davies et al. (2011, hereafter LD11), and we outline the process here. The data were processed using XMM-SASversion 14.0.0, and events lists generated using the EPCHAIN and EMCHAIN tools. Periods of high background levels and particle contamination were excluded using an iterative 3σ clipping process performed on the light curves, and time bins falling outside this range excluded.

Single camera (i.e. PN, MOS1, and MOS2) images and exposure maps were then generated from the cleaned events files, spatially binned with a pixel size of 4.35 arcsec. The images and exposure maps were extracted in the 0.5–2.0 keV band, with individual camera images and exposure maps merged to create a single image per ObsID. The MOS cameras were scaled to the PN by the use of energy conversion factors (ECFs) derived using XSPEC. The ECFs were calculated based upon an absorbed power-law model.

Using the merged images and exposure maps, the XCS Automated Pipeline Algorithm (XAPA) was used for source detection. Once again, full details of the analysis can be found in LD11. XAPA uses a wavelet process based upon the WAVDETECT package (Freeman et al. 2002). Proceeding source detection, detected sources are classified as either point-like or extended. After removal of duplicated sources (i.e. the same sources detected at different epochs), an XCS master source list (MSL) is created. The XCS MSL used in this work contains 338 417 X-ray sources, of which 36 710 are classified as extended.

3.2.2 *DESY3 cross-match with* XMM *archive*

The DESY3 redMaPPer sample defined in Section 2.2 was matched to *XMM* images with the requirement that the redMaPPer position falls within 13 arcmin of the aimpoint of an *XMM* observation. Next, *XMM* images were removed from further analysis based on conditions on the total cleaned exposure time. *XMM* images were removed if, within a 5 pixel radius (centred on the redMaPPer position), the mean exposure time is <3 ks and the median exposure time is <1.5 ks. The median exposure was employed in order to exclude redMaPPer clusters whose X-ray position would be significantly affected by, e.g. chip gaps. Finally, the same exposure cut was carried out at a position $0.8R\lambda$ away from the redMaPPer position (in the direction away from the centre of the *XMM* observation). This is done for two reasons: (i) to reduce the number of clusters near the edge of the field-of-view of *XMM*; and (ii) to encapsulate the miscentring measured between the redMaPPer central galaxy and the X-ray peak position as found in Zhang et al. (2019), and further explored in Section 4. Based on these requirements, there were 1052 DESY3 redMaPPer clusters that fell within the footprint of an *XMM* image (this sample is denoted as the DESY3RM-XMM sample).

3.2.3 *Generation of the DESY3RM-XCS catalogue*

We cross-matched the 1052 DESY3RM-XMM clusters (see Section 3.2.2) with the XCS MSL. At the position of the redMaPPer defined central position, we determine if there is a corresponding XAPA extended source within $2\,h^{-1}$ Mpc, calculated at the redshift of the redMaPPer cluster in question. If an extended source was found, the match was visually inspected to confirm the association of the extended XCS source with the DESY3RM cluster. To perform the inspection process, we inspect both DES Y3 and *XMM* images (examples of which can be found in fig. 2 of Giles et al. 2022). In some cases, the matched X-ray source was in fact associated with another redMaPPer cluster in projection. For these, the redMaPPer cluster in question was labelled as unassociated with the matched X-ray source and classified as undetected. Additionally, in a very small number of cases, it was determined that the match was not associated, but another extended source in the field was, in fact, the X-ray source associated with the redMaPPer cluster. These were manually defined and fed into the final sample of matched sources. The visual inspection process was also used to identify X-ray observations not suitable for further analysis, e.g. effected by periods of high background, these were subsequently removed from further analysis. After this process, confirmed matched redMaPPer clusters are retained, with the sample containing 325 clusters. The remaining 697 DESY3RM clusters have no associated extended X-ray source within $2\,h^{-1}$ Mpc.

As done for the *Chandra* sample (see Section 3.1.3), we further restrict the XMM confirmed matched clusters by removing clusters with a SNR in a 500 kpc aperture less than 9.0, cutting 70 clusters. Finally, only clusters from the volume-limited Y3 redMaPPer catalogue, within $0.2 < z < 0.65$, are retained, resulting in a final sample of 161 clusters.

[3]collected from http://nxsa.esac.esa.int/nxsa-web/

3.2.4 XCS spectral analysis

All *XMM* data were analysed using the XCS Post Processing Pipeline (XCS3P; see LD11 and updates in Giles et al. 2022). Cluster spectra were extracted and fit using XSPEC. The fits are performed in the 0.3–7.9 keV band with an absorbed APEC model (Smith et al. 2001) using the c-statistic (Cash 1979). The abundance was fixed at $0.3 Z_{\odot}$, and the redshift fixed at the value of the redMaPPer defined redshift (note that redshift uncertainties are not taken into account in the fit), leaving the APEC temperature and normalization free to vary. The absorption due to the interstellar medium was taken into account using a multiplicative Tbabs model, with the value of the absorption ($n_{\rm H}$) taken from HI4PI Collaboration et al. (2016) and frozen during the fitting process. The APEC temperature and normalization were free to vary during the fitting process. Temperature errors were estimated using the XSPECERROR command and quoted within 1σ. Finally, luminosities (and associated 1σ errors) were estimated from the best-fit spectra using the XSPECLUMIN command. Spectra for each individual *XMM* camera were extracted, and we filtered out spectra that did not, individually, produce a fitted temperature (complete with 1σ upper and lower limit values) in the range $0.08 < T_{\rm X} < 20$ keV (see Giles et al. 2022, Section 3.1.2). This was performed during each step in the iteration process outlined below.

Spectra are extracted within r_{2500} as done for the MATCha analysis with values estimated using the following equation,

$$E(z)_{r2500} = B_{\delta} \left(\frac{T_{\rm X}}{5\,{\rm keV}} \right)^{\beta}, \quad (1)$$

where $B_{\delta} = 491$ kpc and $\beta = 0.56$, taken from Arnaud et al. (2005). The local background was taken into account using an annulus centred on the cluster with an inner and outer radius of $2r_{2500}$ and $3r_{2500}$, respectively. An initial temperature was calculated within the XAPA defined source region, and this is used to estimate r_{2500} using equation (1). A new $T_{\rm X}$ value is defined within this r_{2500}, and this is in turn used to define a new r_{2500} value. The process was repeated until r_{2500} converged (the ratio of the new to old r_{2500} defined to be >0.9 and <1.1). We required the iteration process to iterate at least three times (irrespective of convergence), up to a maximum of ten iterations. If convergence was not achieved after ten iterations, the process was stopped and no temperature obtained. The same iteration procedure was followed to extract r_{500} temperatures. However, for the r_{500} analysis, the coefficients in equation (1) were $B_{\delta} = 1104$ kpc and $\beta = 0.57$, and the local background used an annulus with an inner and outer radius of $1.05r_{500}$ and $1.5r_{500}$, respectively. For a few clusters with successful r_{2500} the r_{500} fits did not converge, giving a slightly smaller sample for this aperture.

For clusters where the iteration process failed, we estimate a luminosity with a fixed temperature using the process outlined in Giles et al. (2022, Section 3.2). Briefly, the same iteration process is used as above, with the temperature fixed during the fitting process. Initially, a spectrum is extracted, and a temperature of 3 keV was used in the spectral fit to estimate a luminosity. This luminosity was then used to estimate a new temperature using the $L_{\rm X}$–$T_{\rm X}$ relation given in Giles et al. (2022, see table 3). An updated r_{500} is calculated, and the process is repeated until convergence (as above). Lastly, for undetected clusters, we estimate a 3σ upper limit on $L_{\rm X}$ within a 500 kpc aperture with an assumed $T_X = 3$ keV, using the EREGIONANALYSE tool.

4 REDMAPPER CENTRING

RedMaPPer defines the cluster position to be the location of the redMaPPer-determined most likely central galaxy. Both observations and simulations show that, if correctly identified, the central galaxy is a better tracer of the cluster centre of mass or minimum of the gravitational potential than other observable centre measures (e.g. George et al. 2012; Cui et al. 2016). The probability of a given galaxy being the central is calculated based on weights derived from three filters on luminosity, photometric redshift, and local galaxy density (Rykoff et al. 2014). Notably, the central galaxy is not assumed to be the brightest cluster galaxy (BCG); many studies have shown that the BCG is not always the central (Skibba et al. 2011; Zitrin et al. 2012; Hoshino et al. 2015; Lange et al. 2018; De Propris et al. 2021) with non-central fractions of around 30 per cent depending on the method used, halo mass, and BCG luminosity. Based on the cross-correlation with red galaxies and the lensing signals, Hikage et al. (2018) find that the redMaPPer centrals are better tracers of the cluster centre than the brightest member and that the redMaPPer centring probabilities are on average accurate.

In most cases, the redMaPPer most probable central galaxy is the correct central, but in a non-negligible fraction of cases, redMaPPer miscentres choosing the wrong galaxy (Saro et al. 2015; Hollowood et al. 2019; Zhang et al. 2019; Bleem et al. 2020). Miscentring biases the stacked weak lensing cluster mass estimates as well as the measured richnesses, but given a model for miscentring, we can calibrate for these effects. The important parameters here are the fraction of clusters that are miscentred and the distribution of miscentring distances.

4.1 Centring methods

We use the X-ray information to probe miscentring in two ways: first, we measure the offsets between the cluster X-ray peak position and the nominal redMaPPer central galaxy, and model the offset distribution using a two-component model, one for well-centred and one for miscentred clusters. Second, we use the X-ray contours to visually identify the correct central cluster galaxy and compare this to the redMaPPer choice. As detailed in Section 4.2, these methods agree well in terms of the fraction of miscentred clusters and their offset distribution. The X-ray emitting ICM, comprising the bulk of the baryonic component, serves as a good proxy to the gravitational centre of clusters, as the ICM density traces the gravitational potential, and outside of short-lived periods near major mergers, the ICM is largely in hydrostatic equilibrium within this potential.

The X-ray peak to redMaPPer offsets are measured relative to the richness-dependent radius $R_{\lambda} = (\lambda/100)^{0.2}\, h^{-1}$ Mpc. Following Zhang et al. (2019), we model the X-ray peak to redMaPPer central galaxy offset distribution using a two-component model of the form

$$\begin{aligned} P(x|\rho,\sigma,\tau) &= \rho \times P_{\rm cen}(x|\sigma) + (1-\rho) \times P_{\rm mis}(x|\tau), \\ P_{\rm cen}(x|\sigma) &= \frac{1}{\sigma} \exp\left(-\frac{x}{\sigma}\right), \\ P_{\rm mis}(x|\tau) &= \frac{x}{\tau^2} \exp\left(-\frac{x}{\tau}\right). \end{aligned} \quad (2)$$

Here, ρ is the fraction of well-centred clusters, $P_{\rm cen}$ is a Gamma distribution of shape parameter 1, and scale σ representing the offset distribution of well-centred clusters, $P_{\rm mis}$ is a Gamma distribution of shape parameter 2 and scale τ representing the offset distribution of miscentred clusters, and x is the X-ray to redMaPPer position offset normalized by R_{λ}. Some width of the distribution for well-centred

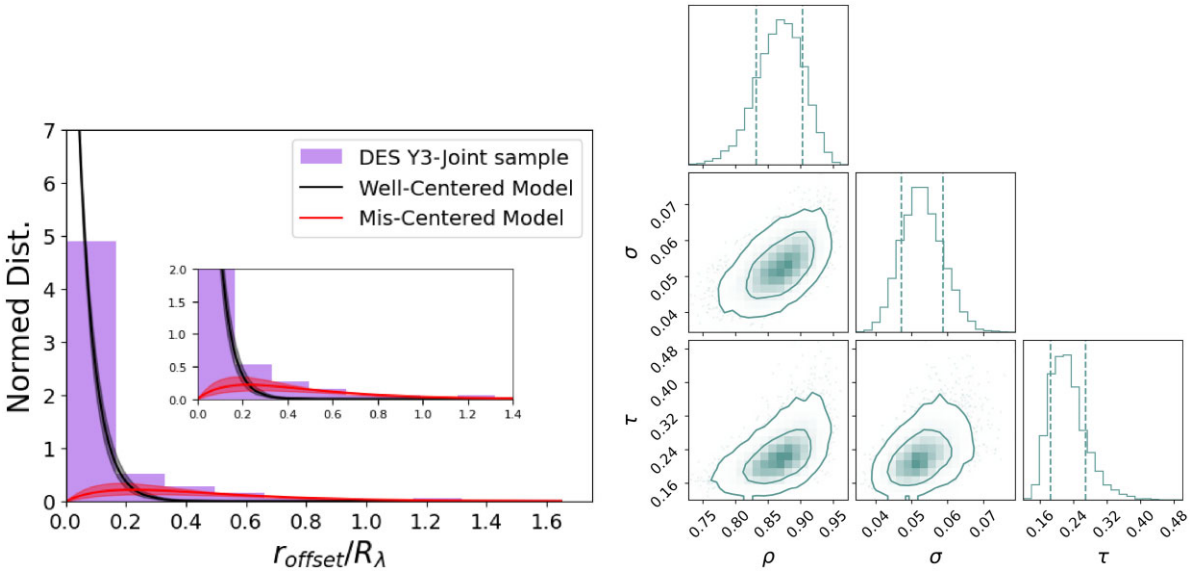

Figure 1. Centring distribution and model fits for the joint *Chandra–XMM* sample. *Left:* Histogram of X-ray peak to redMaPPer position offsets with offsets in terms of $R_\lambda = (\lambda/100)^{0.2} h^{-1}$ Mpc. Overlaid are the best fit models and 1σ uncertainties for the well centred, $P_{\rm cen}$ (black), and miscentred, $P_{\rm mis}$ (pink), distributions. *Right:* Parameter constraint distributions for the centring model fit to the joint cluster sample.

clusters, quantified here by α, is expected due to the finite resolution of both the X-ray and optical images and potential gas-galaxy offsets following mergers. Fits are run using the unbinned data, though the figures show histograms for visualization purposes.

In addition to probing the X-ray to redMaPPer offset, we used the X-ray and DES images to identify, where possible, the correct central cluster galaxy. This analysis revealed the typical reasons for miscentring and allowed us to fit the true central to redMaPPer central distribution for miscentred clusters. Each cluster in the centring samples for both *Chandra* and *XMM* was examined visually using the X-ray contours, DES images, and redMaPPer membership information. Typically, each cluster was looked at by two people, and flagged clusters were additionally checked by TJ. Clusters were flagged if redMaPPer clearly picked the wrong galaxy as the central or if the determination of the central was ambiguous (e.g. there were multiple bright galaxies that could be the central(s)).

The redMaPPer algorithm outputs the positions and centring probabilities of the five most likely central galaxies with the nominal centre taken as the position of the most likely central. For clusters where redMaPPer chose the wrong galaxy, we recorded the DES position of the correct central galaxy and additionally flagged cases where the correct central was one of the other four possible central galaxies identified by redMaPPer and cases, where the correct central was not a candidate member of any redMaPPer cluster. 'Ambiguous' clusters identify those for which it is ambiguous whether the redMaPPer chosen central is correct; in general, there can be cases where the redMaPPer position is clearly wrong but the central galaxy identification is still ambiguous, but for clarity we only list these as miscentred. The designation 'Miscentred' was reserved for cases where redMaPPer clearly chose a galaxy outside of the cluster core or in a clearly subdominant structure outside the main halo.

We note that the methodology for associating X-ray emission to redMaPPer clusters may lead us to miss clusters with very large miscentring distances. In DES Y3, we find one example, missed in both the *Chandra* and *XMM* samples, where Abell 209 is found as a low-richness redMaPPer cluster offset by 2.4 Mpc from the X-ray centre due to gap in the DES data (see fig. 13 of Wetzell et al. 2022).

Table 2. Best fit values and 1σ uncertainties on ρ, σ, and τ for the centring model given by equation (2) for the *Chandra* only, *XMM* only, and joint cluster samples.

Sample	ρ	σ	τ	N
Chandra	0.78 ± 0.06	0.045 ± 0.008	0.21 ± 0.04	124
XMM	0.90 ± 0.04	0.061 ± 0.007	0.24 ± 0.07	161
Joint	0.87 ± 0.04	0.053 ± 0.006	0.23 ± 0.05	243

4.2 Centring results

We first fit the distribution of offsets between the MATCha and XCS determined X-ray peaks and the nominal redMaPPer central galaxy. A histogram of the X-ray peak to redMaPPer offsets is shown in the left-hand panel of Fig. 1. Model parameter constraints for the individual *Chandra* and X*MM* samples are shown in Table 2 and Fig. 2. While the *XMM* sample results in a slightly higher well-centred fraction and width of the well-centred distribution, all of the parameters are consistent between the *Chandra* and *XMM* fits. These fits are also consistent with the DES Y1 *Chandra* and *XMM* fits in Zhang et al. (2019), but with smaller uncertainties given the larger Y3 sample sizes. We also note that σ for the well-centred distribution is significantly larger than the positional uncertainties of *XMM* or *Chandra*.

Given the general consistency, we combine the *Chandra* and *XMM* samples to give a joint sample of 243 clusters once duplicates are removed. For duplicate clusters appearing in both samples, we remove the *XMM* cluster in the joint centring fits given that *Chandra* has superior spatial resolution. For the joint fit, we find a well centred fraction $\rho = 0.87 \pm 0.04$ and a width of the miscentred distribution $\tau = 0.23 \pm 0.05$. The best fit model and distributions of parameter constraints for the joint sample are shown in Fig. 1 and Table 2.

For comparison, Zhang et al. (2019) find $\rho = 0.84^{+0.11}_{-0.08}$ for DES Y1 clusters with *Chandra* observations and $\rho = 0.82^{+0.06}_{-0.06}$ for DES Y1 clusters with *XMM* observations with measured σ's and τ's also consistent with our results. Analysing the offsets between redMaPPer DES Y3 clusters and SPT-SZ positions, Bleem et al. (2020) find $\rho =$

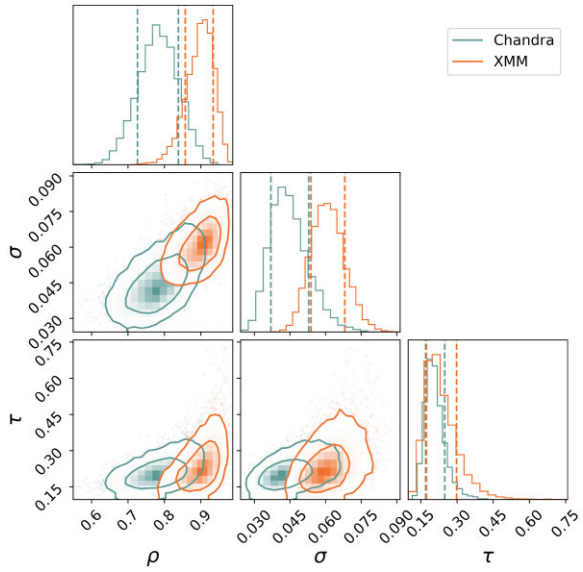

Figure 2. Parameter posterior distributions for the centring model fits to the X-ray peak to redMaPPer position offsets for *Chandra* (blue) and *XMM* (orange).

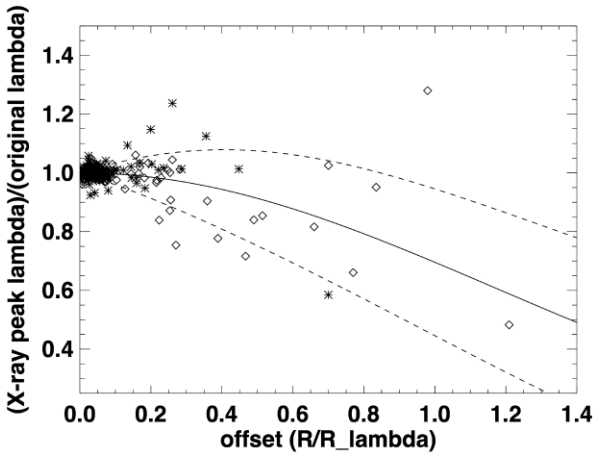

Figure 3. Ratio of the original richness λ at the redMaPPer centre to the richness calculated at the X-ray peak as a function of X-ray peak to redMaPPer offset distance. Clusters in the *Chandra* sample are shown with diamonds, and in the *XMM* sample are shown with asterisks; here for clusters common to the two samples, the *Chandra* position is chosen. The solid line shows the model for DES derived in Zhang et al. (2019), with dashed lines showing the model 1σ dispersion.

$0.87^{+0.02}_{-0.03}$ very similar to what we find, though their $\sigma = 0.12^{+0.02}_{-0.01}$ is significantly higher, potentially due to the poorer resolution of SPT, which has a beam size of 1.3 arcmin (Bleem et al. 2020). They also find a higher $\tau = 0.69^{+0.12}_{-0.09}$ driven by a larger number of clusters with large offsets $> R_\lambda$ in their sample; some of this tail might be due to random associations, but it is also possible that the field-of-view (FOV) of the X-ray instruments and our matching procedure lead us to miss a small fraction of high offset clusters (as noted above). Visual inspection of undetected redMaPPer clusters puts the missed X-ray associations at ∼1 per cent, but this would not catch offsets outside of the X-ray FOV (Zhang et al. 2019). Recently, Seppi et al. (2023) looked at the offsets between eROSITA detected clusters and the redMaPPer centres for redMaPPer run at the X-ray locations. For a sample of 87 eFEDS clusters with $0.15 < z < 0.4$ and $10^{14} < M_{500c} < 8 \times 10^{14} M_\odot$, they find a median X-ray to redMaPPer centre offset of 76^{+30}_{-27} kpc, while for the full eFEDs and eRASS1 samples they find 93^{+44}_{-35} and 159^{+53}_{-58} kpc, respectively. The median offset of our full, joint sample is 102 kpc, fully consistent with these results.

In addition to affecting the stacked lensing signal, miscentring causes a systematic underestimation of cluster richness relative to well-centred clusters, which depends on the miscentring offset. This effect was modelled in Zhang et al. (2019) by fitting the ratio of λ at the nominal centre to λ at the position of the second most likely central galaxy as a function of the offset between the two. We directly probe the richness error by recalculating λ at the X-ray peak position for each cluster in our X-ray centring samples. In Fig. 3, we show the ratio of λ at the X-ray peak to the original redMaPPer λ compared to the Zhang et al. (2019) model. The data are broadly consistent with the model, though with somewhat larger scatter. In general, small offsets of ∼20 per cent of R_λ or less lead to little richness bias, while large offsets can lead to significant underestimation of the richness by 40 per cent or more.

Centring information can also shed light on a particular failure of redMaPPer dubbed *mispercolation* (Hollowood et al. 2019). In cases where two spatially close clusters also have similar richnesses, or when redMaPPer has incorrectly split a large system into multiple clusters, redMaPPer can incorrectly assign a smaller richness to a larger system (and vice versa). Visual inspection enables us to identify these errors in the X-ray data. We correct them following the methods outlined in Hollowood et al. (2019) and Zhang et al. (2019) by manually assigning L_X, T_X, and the centroids and radii of the brightest X-ray cluster to the richest redMaPPer halo and removing the remaining cluster. In this way, we are able to model the mispercolation as an extreme case of miscentring. In the *Chandra* sample, we found only one case of mispercolation, and there were none found in the XMM sample. In general, this failure mode appears to be less frequent for DES than in the SDSS redMaPPer catalogue (Hollowood et al. 2019).

4.2.1 *Origins of miscentring*

Using the identifications of the correct centrals in miscentred clusters, we explore common reasons for miscentring. The numbers of clusters in the categories identified in Section 4.1 for *Chandra*, *XMM*, and the joint sample are listed in Table 3. The designation of 'Miscentred' was relatively robust with independently flagged clusters appearing in both the *Chandra* and *XMM* samples agreeing in all cases but one, marked miscentred for one telescope and ambiguous for the other; this cluster was subsequently moved to ambiguous. The 'Ambiguous' definition was more subjective with four clusters (two each) being flagged for one telescope and not the other; we have left these flags as is and make no strong conclusions based on the ambiguous clusters.

We find that ∼14 per cent of clusters in this sample are miscentred by redMaPPer and an additional ∼7 per cent are ambiguous. These fractions are consistent with the miscentred fractions implied by the X-ray peak to redMaPPer offset distributions shown in Table 2 and Fig. 1 as are the individual *Chandra* and *XMM* fractions. The ambiguous clusters are nearly all merging clusters with multiple substructures each with bright galaxies associated to them. In these cases, the X-ray peak and redMaPPer position sometimes agree while in other cases they pick different substructures, so some fraction of the ambiguous clusters contribute to the X-ray offset distribution. In terms of cluster cosmology the relevant, but unanswerable, question is which substructure in a merger would the simulation's halo finder choose as the cluster centre compared to the

Table 3. Visual classification of redMaPPer centring accuracy using the X-ray surface brightness distribution to identify the central galaxy. Column 2 lists the total number of clusters in each sample; column 3 gives the number of clusters where redMaPPer clearly misidentified the central galaxy, while column 4 lists the number of clusters for which it was ambiguous whether or not the redMaPPer centre was correct. Columns 5 and 6 are subsets of column 3 giving the number of miscentred clusters for which the correct central was one of the possible alternative central galaxies identified by redMaPPer and the number of clusters where the correct central galaxy was not a member of any redMaPPer cluster, respectively.

Source	Total clusters	Miscentred	Ambiguous	Central in top 5	Central not RM member
Chandra	124	21	12	7	12
XMM	161	22	8	11	9
Joint	243	34	17	17	14

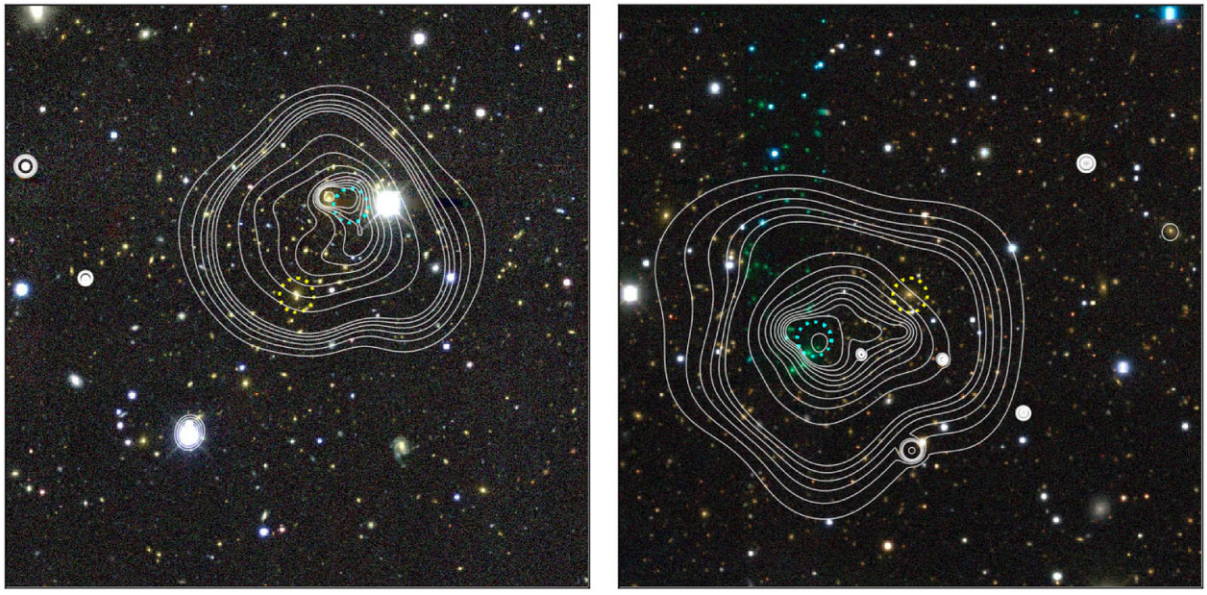

Figure 4. Examples of two clusters where the correct central galaxy was masked in the DES data. Images are 6 × 6 arcmin, *gri* colour composites from DES Y3. Contours show contours of *Chandra* X-ray brightness. The yellow dashed circle marks the galaxy chosen by redMaPPer as the central, and the blue dashed circle is the X-ray peak location. *Left:* MEM_MATCH_ID 403, where the central galaxy is masked by the presence of a bright star. *Right:* MEM_MATCH_ID 559, where the central galaxy is masked due to gaps in the data coverage seen as a strip of green/blue galaxies where data is not available for all bands.

redMaPPer choice. Taking roughly half of the ambiguous fraction is perhaps a good first order estimate of how many of these would be 'miscentred'.

For the miscentred clusters, examination of the DES images in many cases reveals the reasons for miscentring. In a little less than half of the cases, the correct central galaxy is not a member of any redMaPPer cluster, and for two clusters, the correct central was designated as a member of a different cluster by redMaPPer. Of those clusters where the correct central was not a redMaPPer candidate member at all, eight were affected by gaps in the DES data or the presence of a nearby star (in equal proportion) and another one by the presence of a large, very low-redshift galaxy. In these cases, the central was likely masked out. Fig. 4 shows examples of clusters miscentered due to masking. An additional two were affected by AGN or star-formation in the central galaxy, and we note that these cases might be over-represented in our archival X-ray samples. The reasons for miscentring in the remaining four clusters in this category are unclear.

In half of the miscentred clusters, the correct central galaxy was one of the other possible centrals identified by redMaPPer and predominantly the second most likely.

Fig. 5 shows the distribution of offsets between the redMaPPer chosen central and the true central galaxy for the 34 clusters in the joint sample identified visually as miscentred. Fitting the miscentred model $P_{\rm mis}$ to this distrubution, we find $\tau = 0.18 \pm 0.02$, slightly smaller but consistent with what we measure for the X-ray to redMaPPer $P_{\rm mis}$ model.

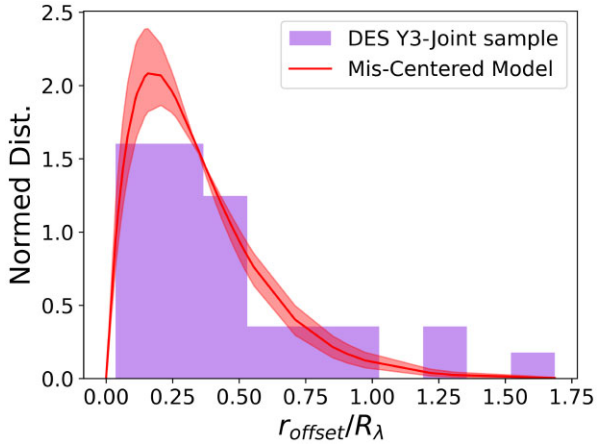

Figure 5. Fit of miscentred clusters only in the joint *Chandra–XMM* sample. Colours are the same as in the left-hand panel of Fig. 1.

Table 4. Best fit values and 1σ uncertainties on ρ, σ, and τ for the centring model given by equation (2) for the low-richness and high-richness samples compared to joint results.

Sample	ρ	σ	τ	N
$20 < \lambda < 40$	0.86 ± 0.05	0.057 ± 0.009	0.26 ± 0.09	82
$\lambda > 40$	0.87 ± 0.05	0.053 ± 0.008	0.24 ± 0.07	161
$20 < \lambda < 75$	0.89 ± 0.04	0.054 ± 0.007	0.24 ± 0.07	131
$\lambda > 75$	0.84 ± 0.06	0.053 ± 0.010	0.25 ± 0.08	112
Full joint sample	0.87 ± 0.04	0.053 ± 0.006	0.23 ± 0.05	243

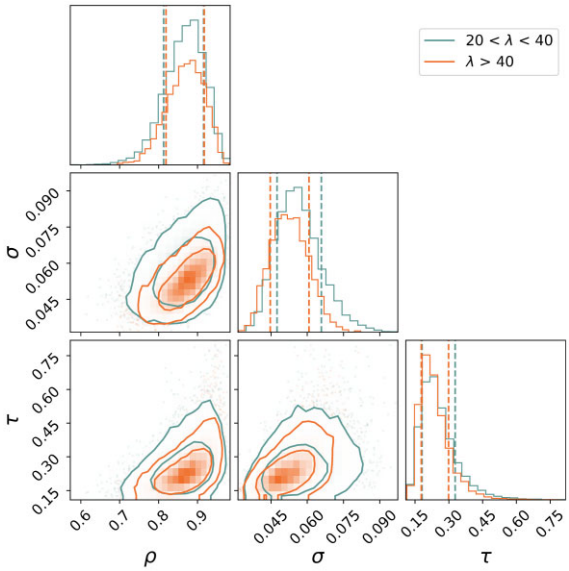

Figure 6. Plots showing the parameter constraint distributions for the joint *Chandra* and *XMM* sample in bins of λ. The $20 < \lambda < 40$ bin is shown in blue, and the $\lambda > 40$ bin is shown in orange.

4.2.2 *Miscentring richness and redshift trends*

The joint *Chandra–XMM* centring sample is large enough for us to begin to investigate trends in miscentring across richness and redshift. We first consider bins in richness and cut the joint centring sample on $20 < \lambda < 40$ ('low-richness') and $\lambda > 40$ ('high-richness'). We do not find significant differences in centring results between our low- and high-richness samples (see Table 4, Fig. 6); in fact the two fits are essentially the same and the same as for the full sample. In addition, the range of redshifts and median redshift of the two samples are similar. A larger miscentring fraction for low-richness clusters might have explained the results of Abbott et al. (2020) which imply the measured lensing signal of low-richness clusters is lower than expected, but this does not seem to be the case in our sample. As our low-richness samples are incomplete, we cannot completely rule out this possibility, but the X-ray undetected, low-richness clusters would need to have significantly worse centring. We also experimented with a somewhat higher richness cut-off λ above and below 75 which gives roughly similar numbers of clusters in the two bins, but again found no significant difference (see see Table 4 and Fig. 7). We note that for the $\lambda > 75$ sample, we detect 95 per cent of the clusters which fall within an existing XMM or Chandra observation, so this sample is essentially complete.

To investigate redshift trends, we again use two bins cut on $0.2 < z < 0.4$ ('low-redshift') and $0.4 < z < 0.65$ ('high-redshift'). The results are shown in Fig. 8 and Table 5. We do find a slight increase in the miscentred fraction for the low-redshift sample compared to the high-redshift sample; however, this discrepancy is within 2σ and coupled with a marginal decrease in the width of the miscentred distribution. We note that the two samples have very similar median richnesses of 58 and 63, respectively, and similar richness ranges.

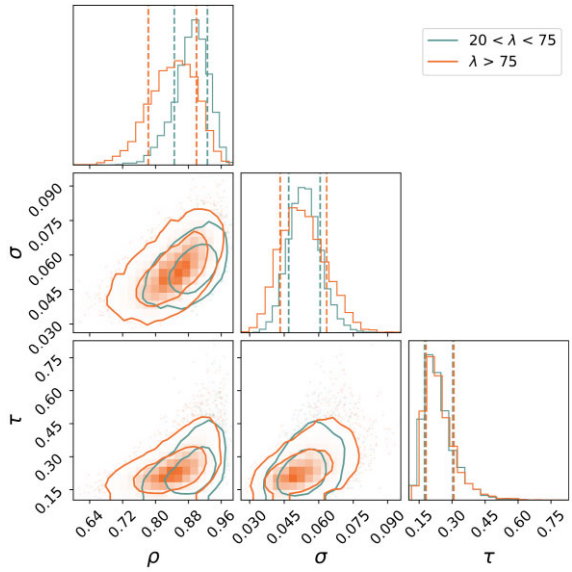

Figure 7. Plots showing the parameter constraint distributions for the joint *Chandra* and *XMM* sample in bins of λ. The $20 < \lambda < 75$ bin is shown in blue, and the $\lambda > 75$ bin is shown in orange.

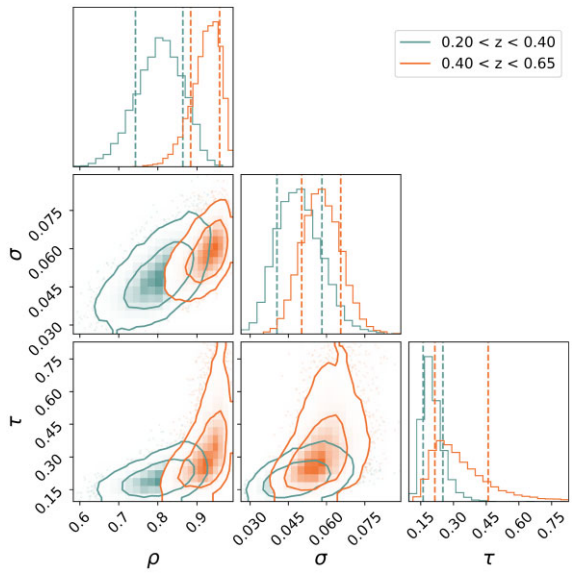

Figure 8. Plots showing the parameter constraint distributions for the joint *Chandra* and *XMM* sample in bins of redshift. The $0.2 < z < 0.4$ bin is shown in blue, and the $0.4 < z < 0.65$ bin is shown in orange.

4.2.3 *Serendipitous versus targeted clusters*

In order to explore potential selection effects, we separated the clusters into those that were the target of the observation and those that were detected 'serendipitously'. In our archival samples, targeted clusters will be biased towards clusters previously know to be X-ray emitting. Serendipitous clusters represent a random selection, though

Table 5. Best fit values and 1σ uncertainties on ρ, σ, and τ the centring model given by equation (2) for the low-redshift and high-redshift samples compared to joint results.

Sample	ρ	σ	τ	N
$0.2 < z < 0.4$	0.80 ± 0.06	0.050 ± 0.009	0.21 ± 0.05	119
$0.4 < z < 0.65$	0.92 ± 0.04	0.058 ± 0.008	0.33 ± 0.13	124
Full joint sample	0.87 ± 0.04	0.053 ± 0.006	0.23 ± 0.05	243

Table 6. Best fit values and 1σ uncertainties on ρ, σ, and τ for the centring model given by equation (2) for serendipitous and targeted clusters.

Sample	ρ	σ	τ	N
Serendipitous	0.87 ± 0.06	0.058 ± 0.009	0.21 ± 0.08	93
Targeted	0.90 ± 0.06	0.070 ± 0.011	0.34 ± 0.15	71

we expect the detected serendipitous clusters to be biased towards those more luminous for their richness. As the *Chandra* sample had relatively few serendipitous clusters, we used only the *XMM* sample in this test.

The results are shown in Table 6. The model fits are completely consistent between the serendipitous and targeted clusters and with the results for the full sample, though the error on the width of the miscentred distribution, τ, is large for the targeted clusters. There is no indication of a bias in the well-centred fraction between targeted and serendipitously observed clusters.

5 RICHNESS SCALING RELATIONS

In this section, we present results from our regression analysis between X-ray properties such as $T_{\rm X}$, $L_{\rm X}$, and richness. All relations reported in this section are found using an analytical program called CluStR,[4] which calls *linmix*, an implementation of the Bayesian regression model introduced in Kelly (2007). The model estimates scaling parameters using data augmentation by incorporating heteroscedastic measurement errors, non-detections, and Gaussian mixture modelling for the covariates. Modelling an appropriate selection function is beyond the scope of this paper, but this is an important limitation to appraise when interpreting the presented scaling relations. However, as noted previously, at $\lambda > 75$ our sample is nearly complete as we detect 95 per cent of the clusters within the archival data used.

5.1 Scaling relation methods

Our results have the form $\ln(y) = \alpha \ln\left(\frac{x}{x_{\rm pivot}}\right) + \beta$, where α, β, and σ are the slope, intercept, and lognormal intrinsic scatter, respectively. The temperature and luminosity errors for all fits are represented as symmetric errors, although asymmetric errors are derived from the X-ray fits. Symmetric errors were chosen due to the limitations of *linmix*, which implements the regression model Kelly (2007). Symmetric errors are calculated, in log space, by averaging the upper and lower errors, and the central value is used as input data point to *linmix*.

In each case, we fit X-ray properties to richness separately for the *Chandra* and *XMM* samples and jointly with the functional form given in equation (3).

$$\ln\left(E(z)^{-\frac{2}{3}} k T_{\rm X,r_{2500}}\right) = \alpha \ln\left(\frac{\lambda_{\rm RM}}{\lambda_{\rm piv}}\right) + \beta. \quad (3)$$

We set the richness pivot point, $\lambda_{\rm piv}$, to 70 and normalize $T_{\rm X}$ as well as $L_{\rm X}$ by appropriate factors of $E(z)$.

For the temperature joint fits, we combine the two samples after adjusting to a common temperature scale and removing duplicates. Here, we keep the *XMM* temperatures for duplicate clusters, given their generally smaller uncertainties. From the 98 galaxy clusters used in the Chandra $T_{\rm X}$ (r_{2500}) sample, we removed 34 duplicate clusters that were present in the *XMM* catalogue in the joint *XMM* and *Chandra* fit. There were 64 remaining galaxy clusters from the Chandra data set that were added to the 160 clusters in the *XMM* data set resulting in 224 total clusters used to determine the joint scaling relation.

To account for the known temperature offset between *Chandra* and *XMM*, we use the 34 clusters present in both samples to derive a relation between the temperatures output by MATCha for *Chandra* observations and those from XCS for *XMM* observations as run on the DES Y3 samples here. We find, for r_{2500} and r_{500} temperatures, respectively,

$$\log_{10}\left(T^{Chandra}_{\rm X,r_{2500}}\right) = 1.01 \log_{10}\left(T^{XMM}_{\rm X,r_{2500}}\right) + 0.10 \quad (4)$$

$$\log_{10}\left(T_{\rm X}, r^{Chandra}_{500}\right) = 1.04 \log_{10}\left(T^{XMM}_{\rm X,r_{500}}\right) + 0.09. \quad (5)$$

These results are consistent with the previous relation derived for SDSS redMaPPer clusters in Rykoff et al. (2016) despite updates in both algorithms and instrument calibrations and our use of a different fitting method. While not directly comparable due to differences in the analysis and methods, the sense and size of the temperature offset we find are similar to what was found by Schellenberger et al. (2015), though our slope is closer to one-to-one with a larger intercept consistent with a constant temperature offset. Before performing the joint *Chandra* + *XMM* $T_{\rm X}$–λ fits, the Chandra temperatures are adjusted to the *XMM* temperature scale.

Several $L_{\rm X,\,r2500}$–$\lambda_{\rm RM}$ fits were conducted following the form of equation (6); in all cases, we use soft band (0.5–2 keV) luminosity and an r_{2500} aperture. Again, we conducted individual *Chandra* and *XMM* fits along with a joint fit. To create the joint sample, duplicate clusters were typically removed from the *Chandra* sample unless the cluster was detected for *Chandra* but not *XMM*. The Chandra and *XMM* luminosities for detected clusters common to both samples are fairly consistent, with the *Chandra* luminosities being on average 6 per cent higher; we rescale the *Chandra* luminosities by this factor in the joint fit,

$$\ln\left(\frac{L_{\rm X,r_{2500}}}{E(z) \cdot 10^{44}\ {\rm ergs\ s^{-1}}}\right) = \alpha \ln\left(\frac{\lambda_{\rm RM}}{\lambda_{\rm piv}}\right) + \beta. \quad (6)$$

5.2 Scaling relation results

Results for $r_{2500} T_{\rm X}$–$\lambda_{\rm RM}$ relation with the cuts mentioned in Section 3.1 are reported in Table 7 and are shown in Fig. 9. The slope and scatter of the $T_{\rm X}$–λ relations for the individual *Chandra* and *XMM* samples are consistent, with the *Chandra* relation having a somewhat shallower slope likely due to the lack of many low-richness clusters in this sample. The normalization of the *Chandra* relations is higher, showing the known offset between *Chandra* and *XMM* temperature estimates (Schellenberger et al. 2015).

Given the general consistency, we combined the two samples to perform a joint *Chandra* + *XMM* $T_{\rm X}$–λ fit in an r_{2500} aperture. We found the slope to be 0.54 ± 0.03, which is consistent with the slope

[4] https://github.com/sweverett/CluStR

Table 7. Parameters for $T_X(r_{2500})$–λ scaling relations. The richness pivot point, λ_{piv}, was set to 70.

Sample	α	β	σ	N
Chandra	0.48 ± 0.08	1.66 ± 0.04	0.25 ± 0.02	98
XMM	0.59 ± 0.03	1.42 ± 0.02	$0.21^{+0.02}_{-0.01}$	160
Joint	0.54 ± 0.03	1.39 ± 0.02	0.22 ± 0.01	224
Joint (λ_{X-ray})	0.56 ± 0.03	1.38 ± 0.02	0.22 ± 0.01	215

of 0.62 ± 0.04 found in Farahi et al. (2019b) for DES Y1. We find the scatter to be 0.22 ± 0.01 while Farahi et al. (2019b) found a somewhat larger scatter of 0.275 ± 0.019.

As discussed in Section 4, the redMaPPer estimated richnesses can be biased low for miscentred clusters. Therefore, we refit the T_X–λ relation using the richnesses calculated centred on the X-ray peak after removing clusters with significant percolation.[5] Table 7 gives the results for the joint *Chandra* and *XMM* fit for an r_{2500} aperture for which the total sample was 215 unique clusters. This fit is very similar to the previous one using the nominal redMaPPer λ.

The scaling relations for the temperature within an r_{500} aperture are reported in Table 8; these results are generally in agreement with those found by Upsdell et al. (2023) for clusters in the XXL and other *XMM* survey regions, despite the use of a different fitting algorithm. However, since many of the clusters studied in Upsdell et al. (2023) are in common with the clusters contained in this work (since they are also derived from the DES Y3 sample), agreement with Upsdell et al. (2023) is expected. We therefore compare the T_X–λ relation presented in Giles et al. (2022), constructed from SDSS redMaPPer clusters with available *XMM* data. The slope of the relation in Giles et al. (2022) is in very good agreement with the results reported in Table 8. Finally, we compare results independent of redMaPPer. Oguri et al. (2018) constructed a sample of clusters using the CAMIRA algorithm run on Hyper-Suprime Cam (HSC) observations. Oguri et al. (2018) investigated the form of the T_X-richness relation using richnesses estimated from CAMIRA and *XMM* temperatures. They found a slope of 0.50 ± 0.12, again consistent with the results given in Table 8.

The $L_{X,r2500}$–λ_{RM} fits were found using soft band (0.5–2 keV) luminosity and an r_{2500} aperture. The results for these fits are reported in Table 9, and shown in Fig. 10. We observe that slope of the *Chandra* sample of 1.36 ± 0.16 is significantly shallower than the slope of the *XMM* sample of 1.95 ± 0.10. The shallower *Chandra* slope is similar to that seen for the temperature fits and again could be because there are relatively few low-richness clusters in the *Chandra* sample. The Chandra L_X–λ relation for detected clusters is very similar the one found by Hollowood et al. (2019) for SDSS redMaPPer clusters.

For the joint *Chandra* + *XMM* L_X–λ fit, we find a slope of 1.86 ± 0.09, consistent with the XMM result, and a scatter of 0.82 ± 0.04. The L_X–λ_{RM} relation considering only detected clusters is prone to selection bias. As a test of the sensitivity of our results, we also fit the L_X–λ_{RM} relation including luminosity upper limits on undetected clusters as censored data (Kelly 2007); specifically, we utilize the 3σ upper limits on the luminosity for undetected clusters, and for detected clusters with SNR < 9, we take the upper limit on the measured luminosity as the censored data point. Including upper limits, we get a joint *Chandra* and *XMM* sample of 676 clusters for

[5]redMaPPer performs a percolation step on clusters close in proximity to avoid double counting galaxies. This step is not implemented in X-ray centred runs where the presence of other clusters is effectively not known.

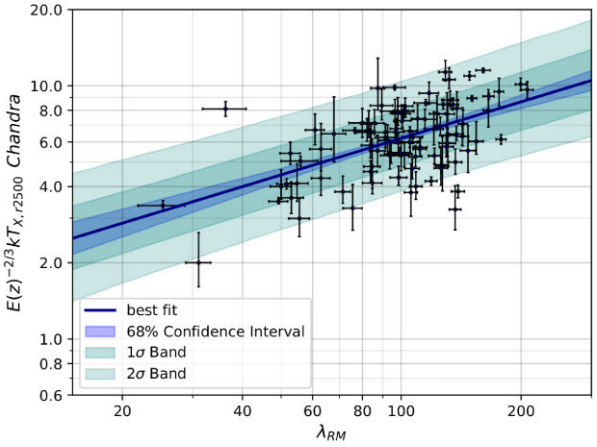

(a) Chandra

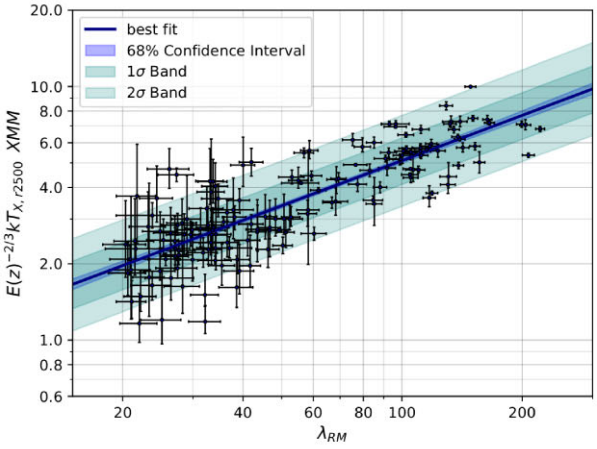

(b) XMM

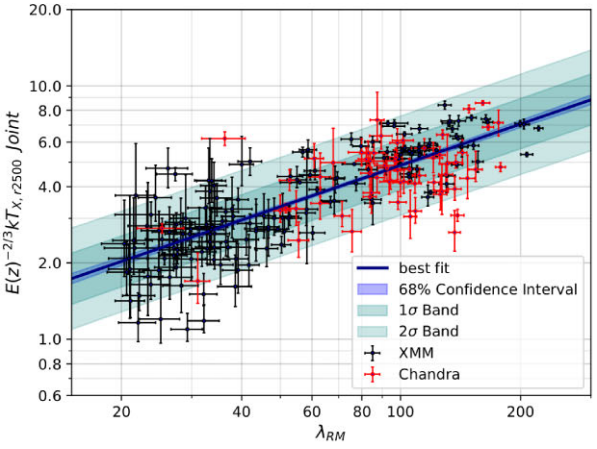

(c) Joint

Figure 9. $T_X(r_{2500})$–λ plots for a) *Chandra*, b) *XMM*, and c) joint *Chandra* and *XMM* samples. For the individual fits, the black points along with their associated errors represent the galaxy clusters from the corresponding data set. For the joint fit, the red points represent the clusters from *Chandra* that were not already catalogued by the *XMM* sample. The dark blue line denotes the best fit, with the richness pivot point set to 70 with the lighter shade of blue representing the 68 per cent confidence intervals on the fit. The 1σ and 2σ scatter are shown in dark green and light green, respectively. In the joint fit, *Chandra* temperatures have been adjusted to the *XMM* temperature scale using equation (4).

Table 8. Parameters for $T_X(r_{500})$–λ scaling relations. The richness pivot point, λ_{piv}, was set to 70.

Sample	α	β	σ	N
Chandra	0.43 ± 0.09	1.72 ± 0.05	0.27 ± 0.03	96
XMM	0.61 ± 0.04	1.39 ± 0.02	0.23 ± 0.02	148
Joint	0.56 ± 0.03	1.38 ± 0.02	0.25 ± 0.02	210

Table 9. Parameters for $L_X(r_{2500})$–λ scaling relations. The richness pivot point, λ_{piv}, was set to 70.

Sample	α	β	σ	N
Chandra	1.36 ± 0.16	0.04 ± 0.08	0.76 ± 0.06	113
XMM	1.95 ± 0.10	-0.38 ± 0.07	0.83 ± 0.05	165
Joint	1.86 ± 0.09	-0.35 ± 0.05	0.82 ± 0.04	239
+ upper limits	1.57 ± 0.06	-0.38 ± 0.05	0.88 ± 0.02	676

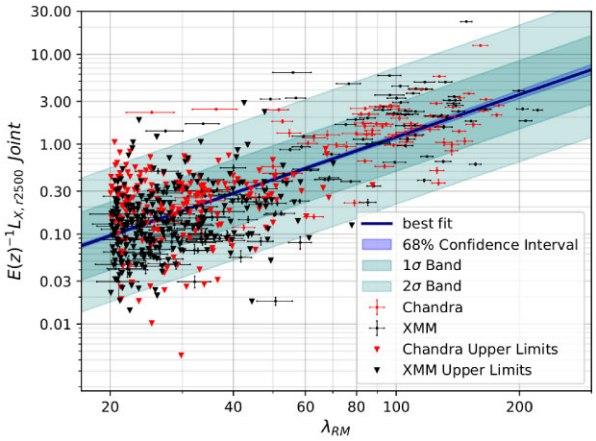

Figure 10. $L_X(r_{2500})$–λ plot for the joint *Chandra* and *XMM* data displayed in red and black, respectively. The repeat observations were examined individually, but generally we chose to keep points from the *XMM* data. For undetected clusters, the 3σ upper limits are displayed with carets. The best-fit line is shown in dark blue; the lighter shade of blue represents the 68 per cent confidence interval on the fit. The 1σ and 2σ scatter regions are shown in dark green and light green, respectively. *Chandra* observations were scaled by 0.94 to match *XMM* based on the per cent difference between the 39 repeat observations.

which we find a somewhat shallower L_X–λ_{RM} slope of 1.57 ± 0.06 and a marginally larger scatter of 0.88 ± 0.02.

5.2.1 *Redshift trends*

We next explore whether there is evidence of a redshift dependence in the scaling relations within the redshift range adopted for DES cluster cosmology, $0.2 < z < 0.65$. We divide clusters into two, non-overlapping redshift bins of $0.2 < z < 0.4$ and $0.4 \leq z < 0.65$ and refit the X-ray scaling relations. These redshift cuts were chosen to ensure that we had a similar and substantial sample size on both sides. The results can be found in Table 10 and are shown in Fig. 11.

For the T_X–λ relation, we found the scatters were consistent across all redshift bins, but not all of the slopes were. We find that our slope value of 0.60 ± 0.04 from the redshift range $0.2 < z < 0.4$ is larger than our slope value of 0.48 ± 0.04 from the redshift range $0.4 \leq z < 0.65$. The two samples have roughly similar median richnesses of 75 and 65, respectively, and similar richness ranges. Comparing

Table 10. $T_X(r_{2500})$–λ and $L_X(r_{2500})$–λ relations in different redshift bins; all fits use the joint *Chandra* and *XMM* sample, and the luminosity fit includes upper limits for undetected clusters.

Relation	α	β	σ	N
T_X–λ $(0.2 < z < 0.4)$	0.60 ± 0.04	1.38 ± 0.02	0.23 ± 0.02	109
T_X–λ $(0.4 \leq z < 0.65)$	0.48 ± 0.04	1.40 ± 0.02	0.23 ± 0.02	116
L_X–λ $(0.2 < z < 0.4)$	1.79 ± 0.10	-0.45 ± 0.08	0.95 ± 0.05	248
L_X–λ $(0.4 \leq z < 0.65)$	1.45 ± 0.07	-0.35 ± 0.07	0.81 ± 0.03	428

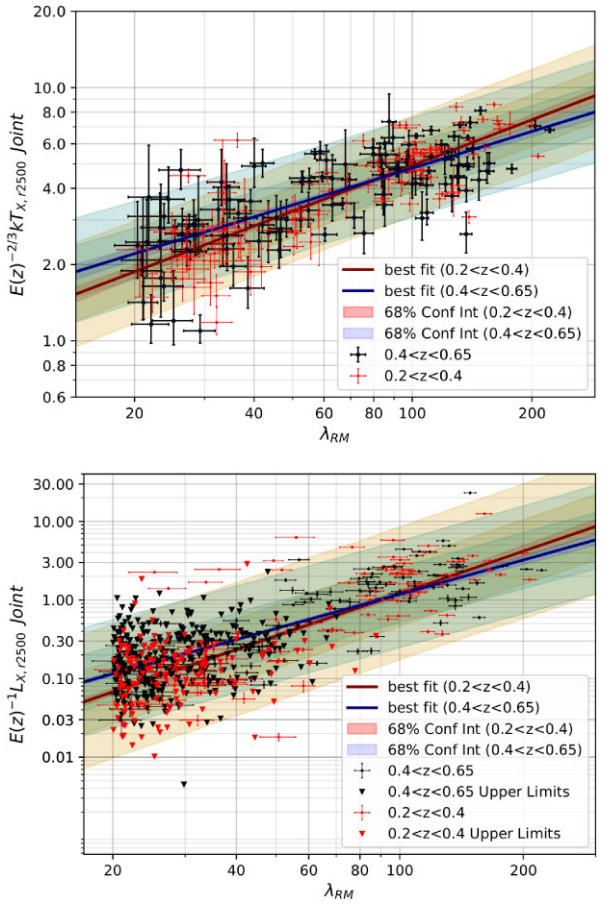

Figure 11. X-ray richness scaling relations in bins of redshift for $T_X(r_{2500})$–λ (top) and $L_X(r_{2500})$–λ (bottom). Red data points and line show clusters in the $0.2 < z < 0.4$ bin and the corresponding best-fit model. The yellow shaded regions show the 1σ and 2σ scatter for the lower-redshift bin. Black data points and the blue line show clusters in the $0.4 < z < 0.65$ bin, and the best-fit model with green shaded regions showing the 1σ and 2σ scatter.

our results to Farahi et al. (2019b), we find a similar slope in the low-redshift bin compared to their reported slope of 0.59 ± 0.05, but a shallower slope in the high-redshift bin compared to the 0.65 ± 0.06 reported in Farahi et al. (2019b).

We observe the same trend of decreasing slope with increasing redshift in the L_X–λ relation including upper limits. This can be seen in our slope value of 1.79 ± 0.10 for our $0.2 < z < 0.4$ bin compared to our slope value of 1.45 ± 0.07 for the $0.4 < z < 0.65$ bin. We also find a marginally significant decrease in the scatter for the high-redshift bin compared to the low-redshift bin. Comparing our results to Hollowood et al. (2019), we see that our low-redshift

Table 11. $T_X(r_{2500})$–λ relation in richness bins; all fits use the joint *Chandra* and *XMM* sample.

Relation	α	β	σ	N
T_X–λ (20 <λ< 40)	0.72 ± 0.32	1.52 ± 0.28	$0.28^{+0.04}_{-0.03}$	73
T_X–λ (λ> 40)	0.49 ± 0.05	1.41 ± 0.02	0.21 ± 0.02	152
T_X–λ (20 < λ < 75)	0.61 ± 0.09	1.42 ± 0.06	0.25 ± 0.02	116
T_X–λ (λ> 75)	0.33 ± 0.09	1.50 ± 0.05	0.21 ± 0.02	109

slope is consistent with their reported slope of 1.78 ± 0.12 for their redshift range of $0.1 < z < 0.35$.

5.2.2 *Richness trends*

Next, we look at the scaling relations in bins of richness. Here, we focus on the T_X–λ relation only; a richness cut in the L_X–λ relation results in selecting primarily detected clusters at high richness and primarily undetected clusters at lower richness. In the presented relations, we tried two different sets of richness bins, first cutting at λ greater than and less than 40 to separate out particularly low-richness clusters, and second cutting at λ of 75 giving bins with relatively equal numbers of clusters. As noted previously, the $\lambda > 75$ sample is also highly complete in that we detect 95 per cent of these clusters that fall within existing *XMM* or *Chandra* data. The results are presented in Table 11 and shown in Fig. 12.

The large uncertainties on the slope and intercept for the lowest-richness bin $20 < \lambda < 40$ preclude us from finding differences from the higher-richness clusters; however, we do find a marginally higher scatter, at about the 2σ level, for these low-richness clusters. These trends are borne out visually in Fig. 12 (a), where there is no indication of a break in the slope, but the low-richness points do appear to have higher scatter compared to the higher-richness clusters. For the higher-richness cut of 75, we do find a mildly steeper slope for the lower-richness $20 < \lambda < 75$ clusters compared to the higher-richness clusters, though in this case, the scatters are similar. While the steeper lower-richness slope mirrors the trend for lower-redshift clusters, we note that the median redshifts of all of our richness bins are similar ($z = 0.40$), as are the redshift ranges.

5.2.3 *Serendipitous versus targeted clusters*

Similar to the test done for centring, we separated the clusters into those that were the target of the observation and those that were detected 'serendipitously' as a test of selection effects in our scaling relations. We again limit this test to the *XMM* sample only, as the *Chandra* sample had relatively few serendipitous clusters with temperature measurements. The results for the $T_X(r_{2500})$–λ relation are presented in Table 12 and Fig. 13.

The scaling relations for the serendipitous and targeted clusters are consistent with the exception that the target clusters have a higher normalization, making them hotter for their richnesses. However, the targeted clusters are also on average richer than the serendipitous sample with median richnesses of 105 and 33 for the target and serendipitous samples, respectively. This trend of higher normalization for targeted clusters was also seen in Giles et al. (2022).

6 DISCUSSION

Our results confirm the generally good performance of the redMaPPer algorithm. Our centring results indicate that less than 21 per cent of redMaPPer clusters are miscentred considering both our visual identifications and the 2σ limit on the well-centred fraction from

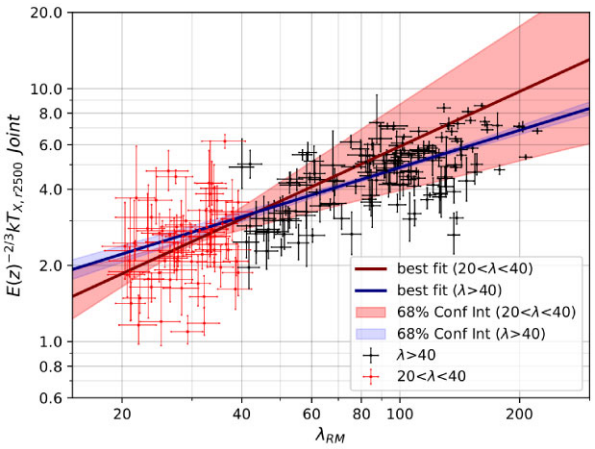

(a) $(20 < \lambda < 40)$ and $(\lambda > 40)$

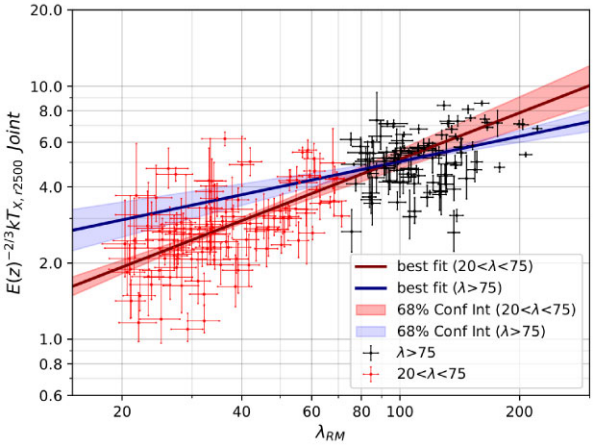

(b) $(20 < \lambda < 75)$ and $(\lambda > 75)$

Figure 12. $T_X(r_{2500})$–λ in bins of richness; the top plot (a) shows the fits for the $20 < \lambda < 40$ and $\lambda > 40$ bins while the bottom plot (b) shows the comparison of $20 < \lambda < 75$ and $\lambda > 75$ clusters. In each case, the red data points and line show clusters in the lower-richness bin and the corresponding best-fit model. Black data points and the blue line show clusters in the higher-richness bin and the best-fit model.

Table 12. $T_X(r_{2500})$–λ relation for the *XMM* sample only separated based on whether the cluster was serendipitous or targeted.

Relation	α	β	σ	N
Serendipitous	0.52 ± 0.07	1.32 ± 0.05	0.18 ± 0.03	89
Targeted	0.45 ± 0.05	1.51 ± 0.03	0.21 ± 0.02	71

modelling the X-ray to redMaPPer offset distribution in our joint sample. Our visual examination revealed that some of the miscentred clusters (∼12 per cent) were due to gaps in the DES Y3 coverage, which will be filled in the final Y6 data set.

We also find a low X-ray temperature-richness scatter of 0.22 ± 0.01. Following the procedure in Farahi et al. (2019b) and using the temperature–mass relation and its scatter from Mantz et al. (2016) and the richness–temperature correlation coefficient from Farahi et al. (2019a), we find a scatter in mass given richness of $\sigma_{\ln M|\lambda} = 0.19 \pm 0.02_{\rm stat} \pm 0.09_{\rm sys}$ with the statistical error arising from uncertainty in the T_X–λ scatter from our fits and the systematic error arising from uncertainties in the mass–temperature scatter and

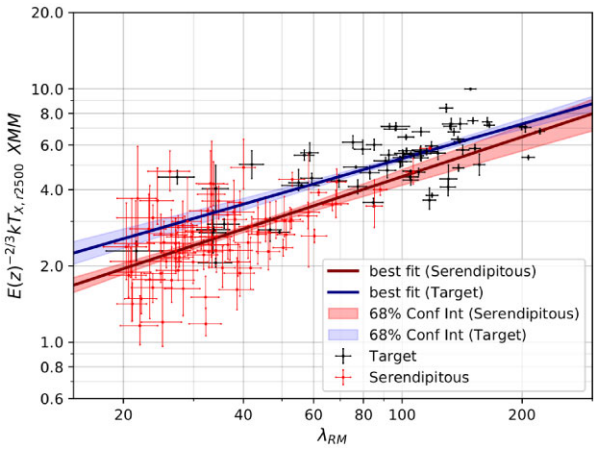

Figure 13. $T_X(r_{2500})$–λ relation for *XMM* detected clusters is only divided according to whether the cluster was the target of the *XMM* observation or if it was serendipitously detected. Red data points and line show serendipitous clusters and their best-fit scaling relation with the 1σ and 2σ scatter in yellow. Black data points and the blue line show targeted clusters and the best-fit model, with green shaded regions showing the 1σ and 2σ scatter.

the richness–temperature correlation. This mass–richness scatter is consistent with the results of Farahi et al. (2019b), but our confidence interval favours lower scatter values.

However, the DES Y1 cluster cosmology results indicate possible unmodelled systematics in the cluster selection, particularly at low richness (Abbott et al. 2020). Miscentring, mass–richness scatter, or contamination that grow as richness decreases could potentially contribute to the results seen in DES Y1. We do see a mildly larger scatter in the T_X–λ relation in our lowest-richness bin, but not a dramatic increase. This conclusion is, of course, limited by the incompleteness of the low-richness sample. We find no indication of an increase in miscetering at lower richnesses, and in fact, the miscentring fraction and distribution are extremely similar in our richness bins. While our archival sample does not have a uniform selection, we find no significant differences in the miscentring or scaling relation scatter for serendipitously detected versus targeted clusters or for the nearly complete high-richness sample compared to lower richnesses, and our results are consistent with previous studies.

Looking at the undetected, serendipitous clusters, we find one significantly underluminous cluster; this $\lambda = 30$ cluster at $z = 0.48$ lies in the same field, but well separated from a high-redshift, Planck cluster with deep *Chandra* data. Two other clusters, one detected and one not, have luminosities or limits just outside of three times the L_X–λ scatter, but this is also about the number we would expect. In general, the depth of the X-ray observations is, in most cases, insufficient to tell whether the undetected clusters are significantly underluminous. Upsdell et al. (2023) come to a similar conclusion considering DES redMaPPer clusters in four contiguous *XMM* survey regions. Looking forward, eROSITA (Merloni et al. 2012), while not generally deeper will provide complete X-ray coverage with a better understood selection function and much higher sample sizes allowing for studies of redMaPPer selection. Targeted *XMM* follow-up of underluminous clusters and stacking analyses can also be instructive.

7 CONCLUSIONS

We investigate the X-ray properties of optically-selected clusters in the first three years of DES data. Specifically, we analyse 676 redMaPPer-selected DES clusters which fall within archival *Chandra* and/or *XMM* observations, of which 239 are detected with SNR > 9 after flag cuts, in order to probe miscentring, richness scatter, and other aspects of redMaPPer selection. Our primary results include:

(i) 10–20 per cent of redMaPPer clusters in this sample are miscentred based on both the X-ray peak to redMaPPer offset distribution and visual inspection.

(ii) The miscentred fraction and typical miscentring distance are consistent in bins of richness and redshift and for serendipitous versus targeted clusters. Given these results and the low miscentring fraction, it is unlikely that miscentring is responsible for the cosmological tension found from DES clusters.

(iii) Of the miscentred clusters in roughly 40 per cent the correct central was not a member of any redMaPPer cluster most frequently due to masking because of gaps in the DES coverage or the presence of a nearby bright object. In two clusters, the presence of an AGN or star formation in the central galaxy caused it to be missed by redMaPPer. In half of the miscentred cases, the correct central was one of the other four possible centrals identified by redMaPPer.

(iv) Miscentring can lead to underestimates of cluster richness that become significant for large miscentring distances. Overall, miscentring does not significantly affect the T_X–λ relation, but it does lead to a small number of outliers.

(v) We derive scaling relations between X-ray temperature and luminosity with richness that are generally consistent with previous results.

(vi) We find a $T_X(r_{2500})$–λ scatter of 0.22 ± 0.01 for richness calculated at the X-ray peak, and use this to estimate a scatter in mass given richness of $\sigma_{\ln M|\lambda} = 0.19 \pm 0.02_{\rm stat} \pm 0.09_{\rm sys}$.

(vii) We find a mildly shallower slope of the T_X–λ and L_X–λ relations for higher-redshift clusters ($0.4 < z < 0.65$) than for lower-redshift clusters ($0.2 < z < 0.4$). We also see a mildly larger scatter for low-richness ($20 < \lambda < 40$) compared to higher-richness ($\lambda > 40$) clusters in the T_X–λ relation. The slope and scatter of the T_X–λ relation are consistent within the errors for serendipitous versus targeted clusters.

(viii) While we see one significantly underluminous cluster given its richness, in general for undetected, serendipitous clusters the X-ray data is not deep enough to probe the purity of low-richness redMaPPer clusters.

We note that while at $\lambda > 75$, we detect 95 per cent of the clusters that fall within an existing *XMM* or *Chandra* observation, our sample is substantially less complete at lower richnesses with unknown selection function, so care should be taken in interpreting these results. None the less, we do not find large differences in centring or scaling relation scatter for low versus high richness clusters or serendipitous versus targeted clusters, and only marginally larger scatter when including upper limits on non-detections in the T_X–λ relation.

Looking forward, LSST and Euclid will provide enormous cluster samples out to much higher redshifts, while eROSITA is providing all-sky X-ray coverage. The utility of optical cluster samples, whether selected by redMaPPer or other cluster finders, will continue to depend on multiwavelength follow up like the work presented here to calibrate cluster selection. X-ray and SZ-selected cluster samples rely on optical confirmation, redshifts, and lensing, making understanding the optical data important for these studies as well. The large samples present a challenge for follow-up efforts, and we are continuing to automate our analysis including many aspects of the visual checking and expanding to the use of eROSITA data.

ACKNOWLEDGEMENTS

This work was supported by the U.S. Department of Energy, Office of Science, Office of High Energy Physics, under Award Numbers DE-SC0010107 and A00-1465-001. Funding for the DES Projects has been provided by the U.S. Department of Energy, the U.S. National Science Foundation, the Ministry of Science and Education of Spain, the Science and Technology Facilities Council of the United Kingdom, the Higher Education Funding Council for England, the National Center for Supercomputing Applications at the University of Illinois at Urbana-Champaign, the Kavli Institute of Cosmological Physics at the University of Chicago, the Center for Cosmology and Astro-Particle Physics at the Ohio State University, the Mitchell Institute for Fundamental Physics and Astronomy at Texas A&M University, Financiadora de Estudos e Projetos, Fundação Carlos Chagas Filho de Amparo à Pesquisa do Estado do Rio de Janeiro, Conselho Nacional de Desenvolvimento Científico e Tecnológico and the Ministério da Ciência, Tecnologia e Inovação, the Deutsche Forschungsgemeinschaft and the Collaborating Institutions in the DES.

The Collaborating Institutions are Argonne National Laboratory, the University of California at Santa Cruz, the University of Cambridge, Centro de Investigaciones Energéticas, Medioambientales y Tecnológicas-Madrid, the University of Chicago, University College London, the DES-Brazil Consortium, the University of Edinburgh, the Eidgenössische Technische Hochschule (ETH) Zürich, Fermi National Accelerator Laboratory, the University of Illinois at Urbana-Champaign, the Institut de Ciències de l'Espai (IEEC/CSIC), the Institut de Física d'Altes Energies, Lawrence Berkeley National Laboratory, the Ludwig-Maximilians Universität München and the associated Excellence Cluster Universe, the University of Michigan, NSF's NOIRLab, the University of Nottingham, The Ohio State University, the University of Pennsylvania, the University of Portsmouth, SLAC National Accelerator Laboratory, Stanford University, the University of Sussex, Texas A&M University, and the OzDES Membership Consortium.

Based in part on observations at Cerro Tololo Inter-American Observatory at NSF's NOIRLab (NOIRLab Prop. ID 2012B-0001; PI: J. Frieman), which is managed by the Association of Universities for Research in Astronomy (AURA) under a cooperative agreement with the National Science Foundation.

The DES data management system is supported by the National Science Foundation under Grant Numbers AST-1138766 and AST-1536171. The DES participants from Spanish institutions are partially supported by MICINN under grants ESP2017-89838, PGC2018-094773, PGC2018-102021, SEV-2016-0588, SEV-2016-0597, and MDM-2015-0509, some of which include ERDF funds from the European Union. IFAE is partially funded by the CERCA program of the Generalitat de Catalunya. Research leading to these results has received funding from the European Research Council under the European Union's Seventh Framework Program (FP7/2007-2013) including ERC grant agreements 240672, 291329, and 306478. We acknowledge support from the Brazilian Instituto Nacional de Ciência e Tecnologia (INCT) do e-Universo (CNPq grant 465376/2014-2).

This manuscript has been authored by Fermi Research Alliance, LLC under Contract No. DE-AC02-07CH11359 with the U.S. Department of Energy, Office of Science, Office of High Energy Physics.

DATA AVAILABILITY

The Chandra and XMM catalogues are available in full in machine readable format. The data underlying this paper are available at https://des.ncsa.illinois.edu/releases/dr2/dr2-docs and https://docs.datacentral.org.au/ozdes/overview/ozdes-data-release/. The redMaPPer catalogue used is proprietary to the Dark Energy Survey Collaboration, but will be released upon publication of the Y3 cluster cosmology papers.

REFERENCES

Abbott T. M. C. et al., 2020, Phys. Rev. D, 102, 023509
Allen S. W., Evrard A. E., Mantz A. B., 2011, ARA&A, 49, 409
Anders E., Grevesse N., 1989, Geochim. Cosmochim. Acta, 53, 197
Arnaud K. A., 1996, in Jacoby G. H., Barnes J., eds, ASP Conf. Ser. Vol. 101, XSPEC: The First Ten Years, p. 17
Arnaud M., Pointecouteau E., Pratt G. W., 2005, A&A, 441, 893
Blackburn J. K., Shaw R. A., Payne H. E., Hayes J. J. E., Heasarc, 1999, FTOOLS: A general package of software to manipulate FITS files, record (ascl:9912.002)
Bleem L. E. et al., 2020, ApJS, 247, 25
Cash W., 1979, ApJ, 228, 939
Costanzi M. et al., 2019, MNRAS, 482, 490
Costanzi M. et al., 2021, Phys. Rev. D, 103, 043522
Cui W. et al., 2016, MNRAS, 456, 2566
De Propris R. et al., 2021, MNRAS, 500, 310
Dickey J. M., Lockman F. J., 1990, ARA&A, 28, 215
Drlica-Wagner A. et al., 2018, ApJS, 235, 33
Farahi A., Evrard A. E., Rozo E., Rykoff E. S., Wechsler R. H., 2016, MNRAS, 460, 3900
Farahi A. et al., 2019a, Nature Communications, 10, 2504
Farahi A. et al., 2019b, MNRAS, 490, 3341
Flaugher B. et al., 2015, AJ, 150, 150
Freeman P. E., Kashyap V., Rosner R., Lamb D. Q., 2002, ApJS, 138, 185
Fruscione A. et al., 2006, in Silva D. R., Doxsey R. E., eds, Proc. SPIE, CIAO: Chandra's data analysis system, p. 62701V
George M. R. et al., 2012, ApJ, 757, 2
Giles P. A. et al., 2022, MNRAS, 516, 3878
Grandis S. et al., 2021, MNRAS, 504, 1253
HI4PI Collaboration et al., 2016, A&A, 594, A116
Hikage C., Mandelbaum R., Leauthaud A., Rozo E., Rykoff E. S., 2018, MNRAS, 480, 2689
Hollowood D. L. et al., 2019, ApJS, 244, 22
Hoshino H. et al., 2015, MNRAS, 452, 998
Huterer D., Shafer D. L., 2018, Rep. Prog. Phys., 81, 016901
Kalberla P. M. W., Burton W. B., Hartmann D., Arnal E. M., Bajaja E., Morras R., Poeppel W. G. L., 2005, A&A, 440, 775
Kelly B. C., 2007, ApJ, 665, 1489
Kirby M. et al., 2019, preprint (arXiv:1910.13548)
Kravtsov A. V., Borgani S., 2012, ARA&A, 50, 353
Lange J. U., van den Bosch F. C., Hearin A., Campbell D., Zentner A. R., Villarreal A. S., Mao Y.-Y., 2018, MNRAS, 473, 2830
Lloyd-Davies E. J. et al., 2011, MNRAS, 418, 14
Mantz A. B. et al., 2016, MNRAS, 463, 3582
McClintock T. et al., 2019, MNRAS, 482, 1352
Merloni A. et al., 2012, preprint (arXiv:1209.3114)
Mulroy S. L. et al., 2019, MNRAS, 484, 60
Myles J. et al., 2021, MNRAS, 505, 33
Oguri M. et al., 2018, PASJ, 70, S20
Romer A. K., Viana P. T. P., Liddle A. R., Mann R. G., 2001, ApJ, 547, 594
Rozo E. et al., 2009, ApJ, 703, 601
Rykoff E. S. et al., 2014, ApJ, 785, 104
Rykoff E. S. et al., 2016, ApJS, 224, 1
Saro A. et al., 2015, MNRAS, 454, 2305
Schellenberger G., Reiprich T. H., Lovisari L., Nevalainen J., David L., 2015, A&A, 575, A30
Seppi R. et al., 2023, A&A, 671, A57
Sevilla-Noarbe I. et al., 2021, ApJS, 254, 24
Skibba R. A., van den Bosch F. C., Yang X., More S., Mo H., Fontanot F., 2011, MNRAS, 410, 417

Smith R. K., Brickhouse N. S., Liedahl D. A., Raymond J. C., 2001, ApJ, 556, L91
Upsdell E. W. et al., 2023, MNRAS, 522, 5267
Weinberg D. H., Mortonson M. J., Eisenstein D. J., Hirata C., Riess A. G., Rozo E., 2013, Phys. Rep., 530, 87
Wetzell V. et al., 2022, MNRAS, 514, 4696
Zhang Y. et al., 2019, MNRAS, 487, 2578
Zitrin A., Bartelmann M., Umetsu K., Oguri M., Broadhurst T., 2012, MNRAS, 426, 2944

SUPPORTING INFORMATION

Supplementary data are available at *MNRAS* online.

suppl_data

Please note: Oxford University Press is not responsible for the content or functionality of any supporting materials supplied by the authors. Any queries (other than missing material) should be directed to the corresponding author for the article.

APPENDIX A: APPENDIX A: CHANDRA AND XMM CATALOGS

Tables A1 and A2 display the properties of the galaxy clusters from the *XMM* and *Chandra* samples, respectively. The identification for each galaxy is represented in the 'Name' column, followed by the redMaPPer Mem Match ID, redMaPPer position, richness, redshift, positions of the X-ray peak, the 500 kiloparsec SNR, X-ray observations, and a column to identify serendipitous clusters. Table A2 has two additional columns to identify the clusters used in the centring analysis and scaling relations.

Table A1. Provided is a sample of *XMM* galaxy cluster properties. All X-ray temperatures are in units of keV and all X-ray luminosities are in units of 10^{44} ergs s^{-1}. The clusters are identified by their 'Name' in the first column followed by their 'Mem Match ID' in ascending order. The 'RA RM' and 'Dec RM' columns give the redMaPPer position of the bright central galaxy while 'RA pk' and 'Dec pk' give the location of the X-ray peak in each cluster. The richnesses and the 1σ richness errors of the clusters are in the 'λ' and 'λ err' columns. Following is 'z', the redshift column. The 500 kiloparsec SNR is in the '500 kpc SNR' column. The X-ray temperatures found in an r_{2500} aperture along with the lower and upper 1σ uncertainties are in the '$T_{x,r2500}$', '$T_{x,r2500}-$', and '$T_{x,r2500}+$' columns. Similarly, the X-ray temperatures with uncertainty found in an r_{500} aperture are in the '$T_{x,r500}$', '$T_{x,r500}-$', and '$T_{x,500}+$' columns. The soft band luminosities are in the '$L_{x,r2500}$' column, followed by the lower and upper 1σ uncertainties in '$L_{x,r2500}-$' and '$L_{x,r2500}+$', respectively. the column titled 'serend' identifies if a galaxy cluster was found serendipitously. The full catalogue of detected *XMM* clusters is available in full in machine readable format.

Name	Mem Match ID	RA RM	Dec RM	λ	λ err	z	RA pk	Dec pk	500 kpc SNR
RMJ0254015.5-585710.65	1	43.5646	−58.953	221.674	5.713	0.428	43.570	−58.9499	9.865
RMJ053255.66-370136.08	2	83.2319	−37.0267	199.432	5.879	0.287	83.2345	−37.0283	50.360
RMJ230822.21-021131.69	3	347.0926	−2.1921	163.583	4.295	0.294	347.0926	−2.1922	39.792
RMJ051637.36-543001.65	4	79.1557	−54.5005	207.243	7.181	0.299	79.1583	−54.5145	63.349
RMJ024524.81-530145.39	8	41.3534	−53.0293	150.571	4.141	0.300	41.3633	−53.0314	57.125
$T_{x,r2500}$	$T_{x,r2500}-$	$T_{x,r2500}+$	$T_{x,r500}$	$T_{x,r500}-$	$T_{x,r500}+$	$L_{x,r2500}$	$L_{x,r2500}-$	$L_{x,r2500}+$	serend
7.910	0.180	0.181	7.373	0.188	0.188	2.998	0.019	0.020	0
7.828	0.218	0.220	7.527	0.247	0.247	4.549	0.036	0.034	0
8.187	0.310	0.313	8.055	0.375	0.375	2.788	0.030	0.028	0
5.936	0.114	0.115	5.758	0.113	0.113	2.120	0.012	0.013	0
8.293	0.209	0.210	8.181	0.282	0.281	4.384	0.029	0.029	0

Table A2. *Chandra* galaxy cluster and their properties. All of the column names are identical to those found in Table A1 with an addition of the columns 'scaling' and 'centring' at the end to represent, which clusters were used in the centring analysis and the scaling relations. The full catalogue of detected *Chandra* clusters is available in full in machine readable format.

Name	Mem match ID	RA RM	Dec RM	λ	λ err	z	RA pk	Dec pk	500 kpc SNR
RMJ053255.66-370136.08	2	83.2319	−37.0267	199.432	5.879	0.283	83.2325	−37.0265	94.277
RRMJ230822.21-021131.69	3	347.0926	−2.1921	163.583	4.295	0.293	347.0920	−2.1912	136.880
RMJ051637.36-543001.65	4	79.1557	−54.5005	207.243	7.181	0.299	79.1511	−54.5085	58.488
RMJ041110.97-481939.64	6	62.7957	−48.3277	178.045	5.029	0.413	62.8166	−48.3131	78.698
RMJ232511.72-411213.33	7	351.2988	−41.2037	176.001	4.716	0.358	351.2995	−41.2023	39.184

$T_{x,r2500}$	$T_{x,r2500}-$	$T_{x,r2500}+$	$T_{x,r500}$	$T_{x,r500}-$	$T_{x,r500}+$	$L_{x,r2500}$	$L_{x,r2500}-$	$L_{x,r2500}+$	serend	scaling	centre
11.166	0.638	0.642	10.934	0.858	0.857	4.944	0.069	0.068	0	1	1
nan	nan	nan	nan	nan	nan	2.908	0.021	0.021	0	1	1
10.675	0.816	0.822	14.845	1.184	2.39	3.052	0.052	0.052	0	1	1
7.107	0.312	0.318	nan	nan	nan	3.555	0.061	0.061	0	1	1
10.74	1.318	1.398	12.806	1.89	3.419	2.702	0.083	0.084	0	1	1

[1]*University of California, Santa Cruz, Santa Cruz, CA 95064, USA*
[2]*University of California, Davis, 1 Shields Ave, Davis, CA 95616, USA*
[3]*Santa Cruz Institute for Particle Physics, Santa Cruz, CA 95064, USA*
[4]*SLAC National Accelerator Laboratory, 2575 Sand Hill Road, Menlo Park, CA 94025, USA*
[5]*Swinburne University of Technology, John St, Hawthorn VIC 3122, Australia*
[6]*Department of Physics and Astronomy, Pevensey Building, University of Sussex, Brighton, BN1 9QH, UK*
[7]*Centre National d'Études Spatiales (CNES), 2, place Maurice-Quentin 75039, Paris, France*
[8]*Jet Propulsion Laboratory, California Institute of Technology, 4800 Oak Grove Dr, Pasadena, CA 91109, USA*
[9]*Departments of Statistics and Data Science, University of Texas at Austin, Austin, TX 78757, USA*
[10]*Kavli Institute for Particle Astrophysics & Cosmology, P. O. Box 2450, Stanford University, Stanford, CA 94305, USA*
[11]*SLAC National Accelerator Laboratory, Menlo Park, CA 94025, USA*
[12]*Los Altos High School , 201 Almond Ace, Los Altos, CA 94022, USA*
[13]*University of California, Berkeley, University Avenue and, Oxford St, Berkeley, CA 94720, USA*
[14]*University Observatory, Faculty of Physics, Ludwig-Maximilians-Universität, Scheinerstr. 1, D-81679 Munich, Germany*
[15]*Institute of Space Sciences (ICE, CSIC), Campus UAB, Carrer de Can Magrans, s/n, E-08193 Barcelona, Spain*
[16]*Homestead High School , 21370 Homestead Rd, Cupertino, CA 95014, USA*
[17]*De Anza College, 21250 Stevens Creek Blvd, Cupertino, CA, USA*
[18]*Department of Physics and Astronomy, Clemson University, Kinard Lab of Physics, Clemson, SC 29634-0978, US*
[19]*California State University San Marcos, 333 S Twin Oaks Valley Rd, San Marcos, CA 92096, USA*
[20]*Dougherty Valley High School , 10550 Albion Rd, San Ramon, CA 94582, USA*
[21]*University of New Hampshire, 105 Main St, Durham, NH 03824, USA*
[22]*Laboratório Interinstitucional de e-Astronomia - LIneA, Rua Gal. José Cristino 77, Rio de Janeiro, RJ – 20921-400, Brazil*
[23]*Fermi National Accelerator Laboratory, P. O. Box 500, Batavia, IL 60510, USA*
[24]*Department of Physics, University of Michigan, Ann Arbor, MI 48109, USA*
[25]*Institute of Cosmology and Gravitation, University of Portsmouth, Portsmouth, PO1 3FX, UK*
[26]*Department of Physics & Astronomy, University College London, Gower Street, London, WC1E 6BT, UK*
[27]*Instituto de Astrofisica de Canarias, E-38205 La Laguna, Tenerife, Spain*
[28]*Universidad de La Laguna, Dpto. Astrofisica, E-38206 La Laguna, Tenerife, Spain*
[29]*Institut de Física d'Altes Energies (IFAE), The Barcelona Institute of Science and Technology, Campus UAB, E-08193 Bellaterra (Barcelona), Spain*
[30]*Astrophysics Research Institute, Liverpool John Moores University, Liverpool Science Park, 146 Brownlow Hill, Liverpool L3 5RF, UK*
[31]*Astronomy Unit, Department of Physics, University of Trieste, via Tiepolo 11, I-34131 Trieste, Italy*
[32]*INAF-Osservatorio Astronomico di Trieste, via G. B. Tiepolo 11, I-34143 Trieste, Italy*
[33]*Institute for Fundamental Physics of the Universe, Via Beirut 2, I-34014 Trieste, Italy*
[34]*Hamburger Sternwarte, Universität Hamburg, Gojenbergsweg 112, D-21029 Hamburg, Germany*
[35]*School of Mathematics and Physics, University of Queensland, Brisbane, QLD 4072, Australia*
[36]*Institute of Theoretical Astrophysics, University of Oslo, P.O. Box 1029 Blindern, NO-0315 Oslo, Norway*
[37]*Kavli Institute for Cosmological Physics, University of Chicago, Chicago, IL 60637, USA*
[38]*Instituto de Fisica Teorica UAM/CSIC, Universidad Autonoma de Madrid, E-28049 Madrid, Spain*
[39]*Center for Astrophysical Surveys, National Center for Supercomputing Applications, 1205 West Clark St, Urbana, IL 61801, USA*
[40]*Department of Astronomy, University of Illinois at Urbana-Champaign, 1002 W. Green Street, Urbana, IL 61801, USA*
[41]*School of Mathematics, Statistics, and Computer Science, University of KwaZulu-Natal, Westville Campus, Durban 4041, South Africa*
[42]*Center for Cosmology and Astro-Particle Physics, The Ohio State University, Columbus, OH 43210, USA*
[43]*Department of Physics, The Ohio State University, Columbus, OH 43210, USA*
[44]*Center for Astrophysics | Harvard & Smithsonian, 60 Garden Street, Cambridge, MA 02138, USA*
[45]*Australian Astronomical Optics, Macquarie University, North Ryde, NSW 2113, Australia*
[46]*Lowell Observatory, 1400 Mars Hill Rd, Flagstaff, AZ 86001, USA*
[47]*George P. and Cynthia Woods Mitchell Institute for Fundamental Physics and Astronomy, and Department of Physics and Astronomy, Texas A&M University, College Station, TX 77843, USA*
[48]*George P. and Cynthia Woods Mitchell Institute for Fundamental Physics and Astronomy, and Department of Physics and Astronomy, Texas A&M University, College Station, TX 77843, USA*
[49]*Centro de Investigaciones Energéticas, Medioambientales y Tecnológicas (CIEMAT), 28040 Madrid, Spain*
[50]*Department of Astronomy, University of Michigan, Ann Arbor, MI 48109, USA*
[51]*Institució Catalana de Recerca i Estudis Avançats, E-08010 Barcelona, Spain*
[52]*Department of Physics, Stanford University, 382 Via Pueblo Mall, Stanford, CA 94305, USA*
[53]*Department of Physics, Carnegie Mellon University, Pittsburgh, Pennsylvania 15312, USA*
[54]*Observatório Nacional, Rua Gal. José Cristino 77, Rio de Janeiro, RJ - 20921-400, Brazil*
[55]*Instituto de Fisica Gleb Wataghin, Universidade Estadual de Campinas, 13083-859, Campinas, SP, Brazil*
[56]*School of Physics and Astronomy, University of Southampton, Southampton, SO17 1BJ, UK*
[57]*Computer Science and Mathematics Division, Oak Ridge National Laboratory, Oak Ridge, TN 37831, USA*
[58]*Instituto de Astrofisica e Ciencias do Espaco, Universidade do Porto, CAUP, Rua das Estrelas, P-4150-762 Porto, Portugal*
[59]*Departamento de Fisica e Astronomia, Faculdade de Ciências, Universidade do Porto, Rua do Campo Alegre, 687, 4169-007 Porto, Portugal*
[60]*Lawrence Berkeley National Laboratory, 1 Cyclotron Road, Berkeley, CA 94720, USA*

This paper has been typeset from a TEX/LATEX file prepared by the author.